東京大学　大学院新領域創成科学研究科 基盤科学研究系物質系専攻
平成 23 年度　修士論文

Transport in $LaTiO_3/SrTiO_3$ nanodot arrays
$LaTiO_3/SrTiO_3$ のナノドットアレー構造の輸送特性

2012 年 1 月 24 日提出
指導教員：Mikk Lippmaa　准教授

47-106015：笹村　謙

Contents

Chapter 1

Introduction

1.1 Research purpose

Transition metal oxides have been a subject active research for more than half a century. Initial applications have been in the area of dielectrics, ferro electrics, and piezoelectric. More recently, magnetism and superconductivity have been the focus of oxide physics research. There are many different ways how the properties of oxides may be controlled. Besides changes in crystal structure and composition, oxides offer numerous other ways to adjust the physical properties, such as doping or various external excitations.

In most compounds, the crystal structure can be assumed to be a fixed parameter. In oxides, however, this is not always true. Many oxide compounds can be viewed along the high-symmetry directions of a crystal as layers of atoms. In a thermodynamic crystal growth process, the types and sequence of atomic layers, or the phase that forms, is determined by the the composition of the source materials and the thermodynamic stability of a structure. By using thin film growth techniques, oxides crystals can often be grown as controlled sequence of individual layers, as long as general charge neutrality of the crystal can be maintained. The boundary between a compound and a heterostructre or a superlattice is thus not as clear as, for example, in semiconductors.

The ability to grow single atomic layers opens up a possibility of designing many new types of crystals, where the crystal properties are determined by the artificially-imposed structure. Some recent examples include two-dimensional superconductivity [22] and metallic quantum wells.[3] Heterostructures can be used as model systems to understand mechanisms that control the distribution of charge in oxides with very large unit cells. Several types of measurements can be used in heterostructures to measure the electronic structure in the interface layers. For example, cross-sectional TEM and electron loss spectroscopy can be used to visualize the spread

of charge at interfaces, [44] while photoemission spectroscopy can be used probing the depth-dependent electronic structures close to a surface. When the local electronic density changes lead to metal-insulator transitions, it is possible to use direct scanning probe techniques to measure the formation of conduction paths or magnetic domains at heterostructre interfaces.[3]

Heterostructures are usually two-dimensional, but this is not strictly necessary. It is possible to use single atomic layer deposition techniques to also grow various fractional structures on crystal surfaces. This type of a fractional heterostructure, with an intentional spatial variation in composition, is the subject this study.

1.2 Measurement mechanism

The experimental methods that can be used to probe the electronic structure at a heterostructure can be roughly divided into out-of-plane and in-plane techniques. The typical out-of-plane techniques can only access the outer surface of a crystal. Measurements like photoelectron spectroscopy, scanning probe imaging, and most electrical characterization can only use the surface of a sample to determine the characteristics of layers that are located below the surface.

In some cases, cross-sectional data can be obtained by looking at the edge of a cleaved or cut heterostructure sample. Although the experiment is technically very challenging, good results have been obtained TEM analysis of slices cut from heterostructure samples.[44, 3]

The idea behind this work is to turn a heterostructure on its side by growing spatially inhomogeneous layers forming arrays of nanodots or nanowires and examining the change of the physical properties by direct surface imaging by atomic force or tunneling microscopies and analyzing the in-plane transport behavior of such nanostructure arrays. In this work, the specific task was to determine the length scale of electron accumulation close to a heavily-doped atomic layer at $SrTiO_3$/$LaTiO_3$ interfaces. Specifically, $LaTiO_3$ nanodots were grown on flat $SrTiO_3$ surfaces, introducing spatially inhomogeneous doped regions, separated by non-doped pristine $SrTiO_3$ terrace regions, as illustrated in Fig.1.1(b)

The effect of the $LaTiO_3$ nanodots is to create an accumulation region of electrons at the interface with $SrTiO_3$. This electron accumulation creates metallic islands within the otherwise insulating surface of a $SrTiO_3$ crystal. The question that the experiments described in this thesis try answer is how far the metallic region extends around a single $LaTiO_3$ nanodot. The main approach is to fabricate an array of $LaTiO_3$ nanodots on an atomically flat $SrTiO_3$ surface and to compare the average dot distance with the in-plane transporties of the dot array. If the critical distance at which conductivity appears can be determined, it would be possible to say how large the charge accumulation width is.

It is known that the lengths scales that need to be measured are on the nanometer scale. It is therefore not practical to use lithographic patterning to obtain the necessary nanogap structures. Instead, the self-organizing nature of a fractional oxide layer is used and various process parameters are used to control the average nanodot size and areal density.

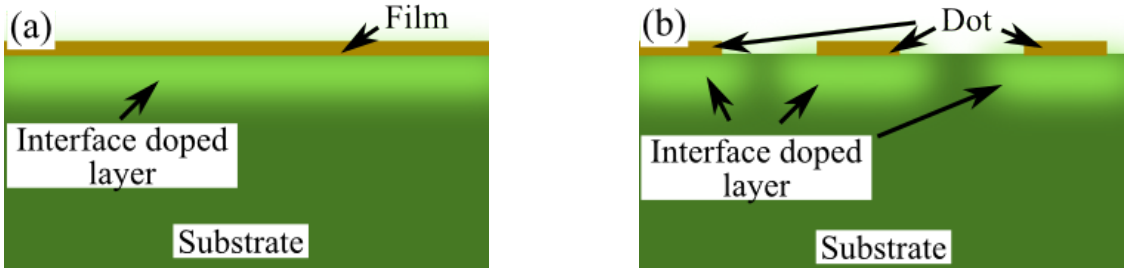

Figure 1.1: Illustration of structures for heterostructure characterization. (a) Normal measurement, (b) nanostructure array measurement.

1.3 Research outline

In this study, $SrTiO_3$ and $LaTiO_3$ were used as the semiconducting substrate and local dopant materials, respectively. Both materials are insulators in bulk form. However, a mixed phase, $(La,Sr)TiO_3$, is a metal due to the fractional filling of the Ti *d* levels. At an interface between $LaTiO_3$ and $SrTiO_3$, conductivity also appears, but because the dopants are spatially restricted, the conductivity is also limited to a thin quasi-two-dimensional layer close to the interface. The dimensionality of the conducting layer depends on the dielectric characteristics of $SrTiO_3$. As the permittivity of $SrTiO_3$ is very high at low temperature, a simple semiconductor picture would predict that an accumulation layer forming in $SrTiO_3$ would be very thick, on the order of tens or even hundreds of nm. However, experiments have shown that while depletion layers do indeed follow the classical semiconductor picture, the actual width of accumulation layers in $SrTiO_3$ can be very small. This behavior has been attributed to the collapse of permittivity under very high electric field conditions, as happens in the interface layers under strong carrier accumulation conditions. Previous experiments by STEM/EELS have shown that the region where Ti valence variations can be detected at a $LaTiO_3/SrTiO_3$ interface is on the order of several unit cells, or about 1 nm.[44] The STEM/EELS experiment, however, can only measure the local valence of Ti, not the actual local conductivity. The purpose of this work is to answer the question about the width of the conducting layer.

To estimate the electron spread in $SrTiO_3$ in the vicinity of $LaTiO_3$ nanodots, the morphology of the nanodots, that is, the average nanodot distance, is determined from scanning probe

topography measurements. This result is correlated with in-plne transport measurements. By fabricating various nanodot arrays with different $LaTiO_3$ dot coverages (Fig.1.2), it should be possible to determine the critical dot distance for metallic conductivity to appear.

It is already known from previous experiments that a critical nanodot coverage of less than one full unit cell exists in this system.[46] In this work, more accurate critical coverage and surface dot morphology are measured by STM topography analysis. The electron spread (accumulation) width is estimated by first measuring the average nanodot spacing from STM images. If the coverage is higher than critical coverage, the nanodot distance would be smaller than the width of electron spread in $SrTiO_3$, and sample would show metallic in-plane conductivity at low temperature. If the coverage is lower than the critical coverage, the electron spread would be smaller than the average nanodot distance, and insulting gaps would thus remain between the metallic islands under the $LaTiO_3$ nanodots. Then sample would in this case be insulating.

Percolation theory can be applied to estimate electron spread (Sec.1.4). The percolation effect at 2 Dimension resistance has already reported [20] Critical rate which can be estimated from percolation theory is critical conductive area. Namely, considering electron spread in $LaTiO_3/SrTiO_3$ structure, it is different that critical coverage of $LaTiO_3$ dot arrow and critical coverage of conductive area at surface. From this difference, electron spread can be estimated.

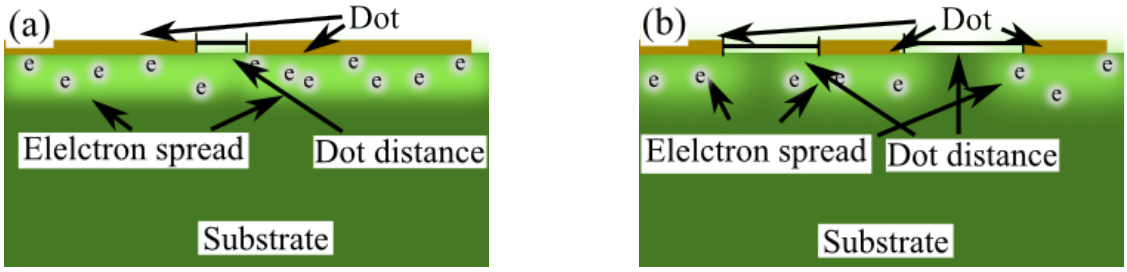

Figure 1.2: Sample structure for measuring the electron spread distance in a metallic nanodot array. (a) Large coverage, metallic conductivity. (b) Small coverage, insulating sample.

1.4 Percolation theory

1.4.1 Concept of percolation

Arrays of metallic nanodots in an insulating substrate is similar to classical problems of percolation. Percolation theory can be used to model various physical properties, such as conductivity in a random structure. For example, Fig. 1.3 shows a classic model of percolation.[64] Black insulating and white metallic balls fill a volume. When bias is applied, percolation models can

be used to predict if current will flow or not, depending on statistical descriptions of the system, such as the ratio of the metallic and insulating balls in the volume under consideration. Obviously, if all balls are metallic current, current will flow. If all balls are insulating, no current will flow. The transition between a metallic to an insulating state will occur at a critical density of metallic balls. Percolation models try to determine this critical behavior. The general conclusion is that conductivity appears if the ratio of metallic particles in a system (p) is over a critical level, p_c. Most importantly, p_c is independent on the ball size.

Percolation theory is widely used in many fields, such as to determine how the degree of polymerization depends on concentration, how the density of trees affects the spread of a forest fire, or how how magnetic properties change when mixing non-magnetic and magnetic materials, etc.[64, 59]

Based on percolation arguments, and considering that a macroscopic nanodot sample is much larger than the individual nanodots, it should be possible to parametrize the conductivity of the system solely in terms of the nanodot coverage, ignoring the nanodot size or shape.

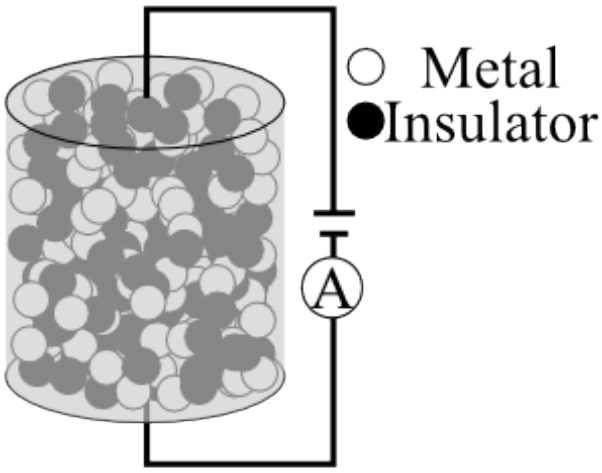

Figure 1.3: Percolation theory model: Insulating (black) and metallic (white) balls fill a volume. Conductivity of the system appears suddenly when the concentration of metallic balls exceeds a critical density.

1.4.2 Detail of percolation theory

The percolation effect is often observed in systems that can be described by a lattice, as in Fig. 1.4. Some lattice points on an infinite grid are filled, possibly forming connected clusters.

The classic problem of metallic and insulating balls in a volume, illustrated in Fig. 1.3, can be replaced with the grid models, with metallic balls being represented by filled points and insulating balls by vacant lattice points. If a connected path extends across the whole grid, the system becomes conducting. The statistical parameters that can be used to describe the system are the probability of occupying a lattice point, p, the number of points in a cluster, s, perimeter length of a cluster, t, and the number of kinds of clusters, $a_{s,t}$, which may be a function of s and t.

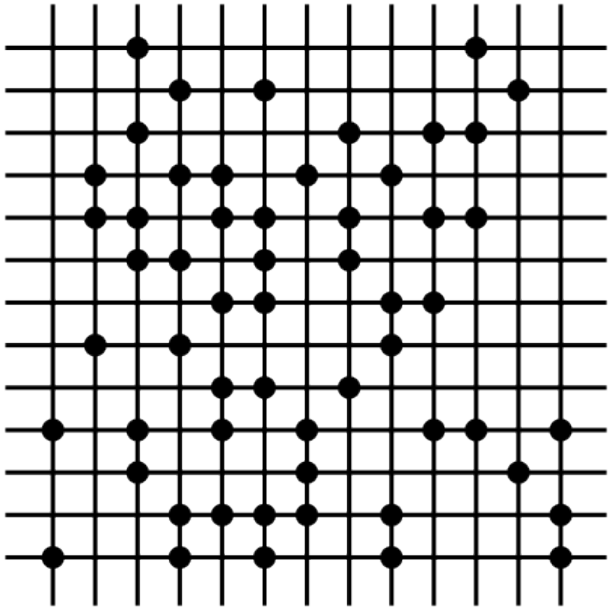

Figure 1.4: A lattice model of percolation: Randomly occupied lattice points led to clustering, finally forming a connected path of occupied points that traverses the grid.

The following parameters are often used to describe a percolation model.

1. $F(p)$: the probability that an arbitrary lattice point belongs to a finite-size cluster.

$$F(p) = \sum_{s,t} a_{s,t} p^s q^s. \tag{1.1}$$

   Here, $q = (1-p)$ is the probability of a point being empty. The sum is over all finite clusters.

2. $P(p)$: probability that a lattice point belongs to an infinite-size cluster that connects to lattice edges for a finite model. This is the percolation probability.

$$P(p) = p - F(p) \tag{1.2}$$

3. $S(p)$: Average size of finite clusters.

$$S(p) = \frac{\sum_{s,t} s a_{s,t} p^s q^t}{\sum_{s,t} a_{s,t} p^s q^t} \tag{1.3}$$

p_c is defined as the critical probability at which infinite clusters form.

P(p) is the most important parameter for analyzing the conductivity in a percolation model. However, conductivity is not directly proportional to $P(p)$, but is usually given by[59, 24]

$$\sigma \sim (p - p_c)^{\mu} \qquad (\mu = 1.2 \sim 1.3) \tag{1.4}$$

where the scaling dependence is often not well understood. [59]

In translating the percolation model to an array of metallic nanodots, the obvious parameters that can be observed is the island size, except that the observed $LaTiO_3$ island size does not correspond exactly to the metallic island size, due to the spread of carriers in the $SrTiO_3$ substrate. However, it is not clear what the influence of the nanodot shape is on the percolation model parameters. For non-circular nanodots, for example, it may be more relevant to parametrize the model not by island size, but by nanodot distances or nanodot connectedness, that is, the number of neighbors that a single nanodot has.

Chapter 2

Equipment and techniques

The fabrication methods and characterization techniques of oxide thin films used in this study are described in this Chapter.

The equipment used in the work can be grouped into four categories: sample fabrication, thin film surface topography measurement, transport measurements, and others supporting tools.

2.1 sample fabrication

2.1.1 Pulsed Laser Deposition(PLD)

Pulsed Laser Deposition(PLD) was used to grow all of the samples used in this work. PLD is a physical vapor deposition technique where a solid target pellet surface is evaporated, or ablated, with a powerful pulsed laser. The pulsed laser beam, usually from a KrF gas excimer laser, is focused on the surface of a target pellet inside a vacuum chamber. The energy density of the laser pulse is sufficient to vaporize almost any material, including high-melting-point oxides. The vapor formed in vacuum is deposited on the surface of a substrate that is positioned so that it faces the target at a distance of a few centimeters. The formation of a hot plasma can be observed visually in the form of a bright ablation plume, as illustrated in Fig. 2.1.

PLD is often used for multi-layer and multi-component oxide thin film growth because a powerful laser can ablate high-melting-point materials and the technique can be used in the presence of a background gas, such as oxygen, at pressures of up to about 1 Torr. The surface temperature of a target reaches several thousand degrees during an ablation pulse, ensuring that all elements evaporate. Due to this PLD gives a nearly one-to-one composition transfer from a ceramic pellet to a growing film, making it a good technique for growing complex oxides.

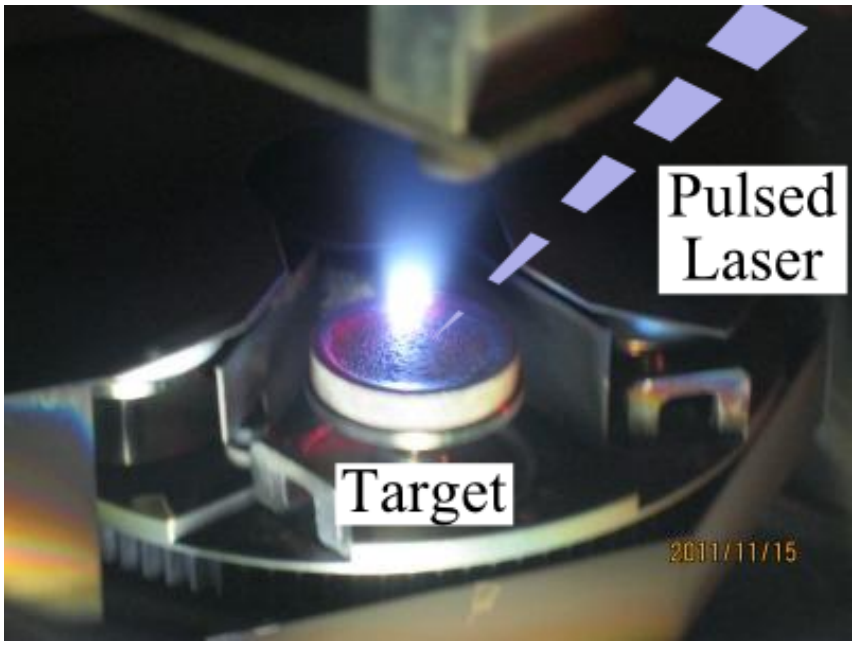

Figure 2.1: A plasma plume formed during the ablation of a $LaTiO_3$ target by a pulsed laser.

Oxygen stoichiometry is an important process parameter for oxide thin film growth. The oxidation of cations in the PLD plume occurs in the gas phase during deposition and, more slowly, on the surface of the film. Since the kinetics of the oxidation process is governed by the ambient oxygen pressure, it is important to choose a suitable oxygen partial pressure for the deposition and annealing of oxide thin films. The PLD chambers used in this work are all basically ultra-high vacuum systems, pumped with turbo molecular pumps, and can reach base pressures on the order of 10^{-9} Torr. The oxygen partial pressure can be adjusted in the chamber anywhere between the base pressure and the atmospheric pressure with the help of several flow restriction valves and manual or piezoelectric gas dosers.When in-situ reflection high-energy electron diffraction (RHEED) is used for monitoring the growth rate or surface roughness of a sample, the chamber pressure is limited to 1 mTorr. A description of real-time growth monitoring can be found in Sec. 2.1.3) Most of the important components of a PLD chamber are shown in a schematic plot in Fig. 2.2.

A powerful pulsed laser is a key element of a PLD system. In this case, a KrF excimer laser was used as the pulsed energy source for ablating a target. The wavelength of a KrF excimer laser is 248 nm and the pulse duration is approximately 20 ns. These parameters are important, because the deep ultraviolet light is necessary to guarantee efficient absorption even in transparent wide-gap oxide materials, such as titanates and aluminates. The relatively long

pulse length is useful for obtaining nearly particle-free evaporation.

Another critical parameter for oxide crystal growth is the growth temperature. Since the melting points of various oxides can be well above 2000 °C, it is easy to see that a wide growth temperature range is advantageous. The PLD systems used here are equipped with semiconductor diode laser heating systems that allow thin films to be grown at temperature of up to about 1200 °C. In laser-heated PLD systems, samples are mounted on a heat-absorbing susceptor, which is heated by a collimated laser beam. Common heat absorbing materials are polycrystalline SiC and oxidized nickel. The wavelength of the heating laser is usually in the 800 to 900 nm range. The susceptor temperature is monitored with an infrared pyrometer and the pyrometer reading is used as a feedback parameter for a computer controlling the heating laser power. This allows the sample temperature to be accurately controlled, while rapid changes are also possible. Details of the optical pyrometry are given in Sec. 4.1.6. The substrate mounting geometry is shown in Fig. 2.3. Sapphire was used as a heat insulator between the heat-absorbing SiC block and the stainless steel body of the sample holder. The substrate crystal was clamped tightly against the SiC susceptor with two stainless steel wires.

Most of the process parameters, such as temperature and pressure, were controlled with the help of a LabVIEW program. The ablation laser energy density, ablation spot size and total pulse energy were set with the help of a single-lens focusing optics and an optical attenuator. The actual excimer laser fluency at the target position was determined by measuring the intensity of laser pulses passing through the chamber. Gradual loss of vacuum viewport transparency due to an accumulation of ablated material could thus be accurately accounted for. [40]

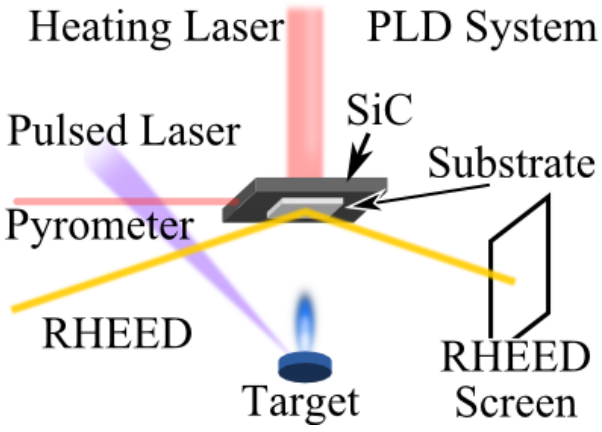

Figure 2.2: A schematic view of the pulsed laser deposition system.

The purpose of the thin film growth experiments was to fabricate fractional oxide layers with different naon-scale feature sizes, such as average nanodot sizes or areal densities. The

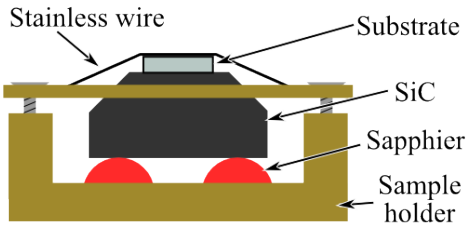

Figure 2.3: Side view of a sample mounted on a SiC heat susceptor.

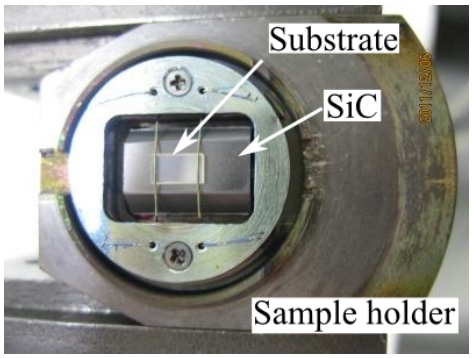

Figure 2.4: Top view of a substrate crystal clamped to a SiC block.

following PLD parameters were used to control the morphology of the fractional layers: **pulsed laser fluence**, **pulse number**, **laser pulse rate**, **substrate temperature**, and **oxygen pressure**.

The pulsed laser fluence is important because the growth rate per pulse and the stoichiometry of the deposited film depend on the laser fluence and the ablation spot size.[41] In general complex oxides tend to show a specific laser fluence where nearly stoichiometric film growth can be achieved. If the fluence deviates from an optimal value, cation non-stoichiometry appears. Perfect cation stoichiometry can be achieved for some oxides, like $LaTiO_3$ or $SrTiO_3$, but may be more problematic in more complex compositions with a larger number of different cation species.

The deposition rate in typical PLD growth is chosen so that a single monolayer is grown with 10 to 100 laser pulses. Changing the laser pulse number is therefore a convenient way of controlling the film thickness with a sub-monolayer accuracy. In addition to counting laser pulses, it is also possible to observe by electron diffraction the periodic surface roughness changes that are related to the formation of individual unit cell layers during layer-by-layer crystal growth. Real-time RHEED oscillation monitoring is useful when the desired film thickness is several unit cells. However, pulse number counting is more useful for nano-structure sample growth where the deposited layer thicknesses are below one monolayer (ML) and complete RHEED intensity oscillations can not be observed. The RHEED monitoring is described in detail in Sec. 2.1.3.

The laser pulse rate can be an important parameter for determining the thin film morphology. Since slow surface rearrangement of adatoms competes with the growth process, it is clear that the deposition rate can affect nanostructure growth. In general, fast growth promotes nucleation and island formation, while slow growth promotes surface flattening. A suitable laser pulse rate is closely linked to the growth temperature, since the surface temperature of a crystal determines

the diffusion rate of atoms on a surface.

The ambient oxygen pressure affects film growth in two ways: a higher background pressure tends to reduce the diffusion length of adatoms on the crystal surface, leading to three-dimensional growth. For some oxides, the oxygen pressure also determines which crystal phase is formed. For example, if $LaTiO_3$ is grown at high oxygen pressures, an insulating oxygen-rich phase may form instead.[45]

2.1.2 Pyrometer

An optical infrared pyrometer is a tool for measuring the temperature of a surface by observing the intensity of the emitted black body radiation. Thermal radiation is always emitted by materials at finite temperatures. the emission energy per unit area per unit time depends on the material temperature. This relationship is described by the Stefan-Boltzmann law (SBL) [21]

$$J = \varepsilon \sigma T^4, \tag{2.1}$$

where J is the emitted energy per unit area and unit time, T is the temperature of a surface, and ε is the emissivity of a surface. For an ideal black body, the emissivity is unity. For other surfaces, emissivities are lower and need to be calibrated. For many semiconductors, the emissivity is also a function of temperature.

The constant σ is the Stefan-Boltzmann constant ($\sigma = \frac{2\pi^5 k_b^4}{15c^2h^3} \simeq 5.67 \times 10^{-8}$ $\mathrm{Wm^{-2}K^{-4}}$, h is the Planck constant, c is the speed of light, and k_b is the Boltzmann constant. Temperature is estimated by a pyrometer based on this equation. The biggest source of errors is caused by the fact the the intensity is usually measured in a single wavelength range while the emissivity is usually not well known. To solve this problem, the emissivity of SiC in the 2 to 2.5 μm range was measured.

2.1.3 Reflection High-Energy Electron Diffraction (RHEED)

PLD chambers often include a Reflection High-Energy Electron Diffraction (RHEED) system for in-situ surface analysis. Surface conditions, such as roughness, in-plane lattice parameter, secondary phase segregation, and the thin film growth rate are commonly measured by RHEED, possibly simultaneously. The grazing-incidence geometry and the ability to operate at gas pressures of up to about 500 mTorr make this technique especially suitable for surface analysis during PLD growth. In this work, the crystal growth mode and growth rate monitoring [30] are the biggest advantages of using RHEED.

There are four main crystal growth modes on a flat step-and-terrace single crystal surface: step flow mode, layer by layer mode, island growth, and 3-dimensional growth on a wetting layer. Especially step-flow and layer-by-layer growth modes are important in this study.

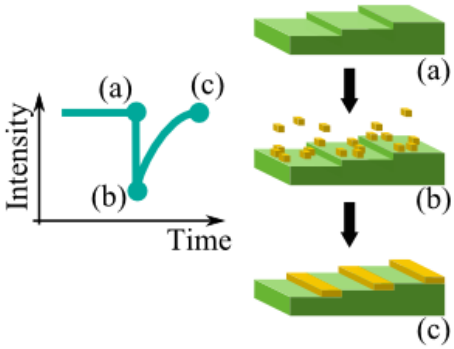

Figure 2.5: Observation of step-flow growth by RHEED.

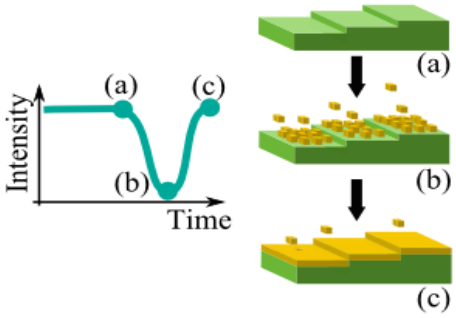

Figure 2.6: RHEED intensity behavior during layer-by-layer growth.

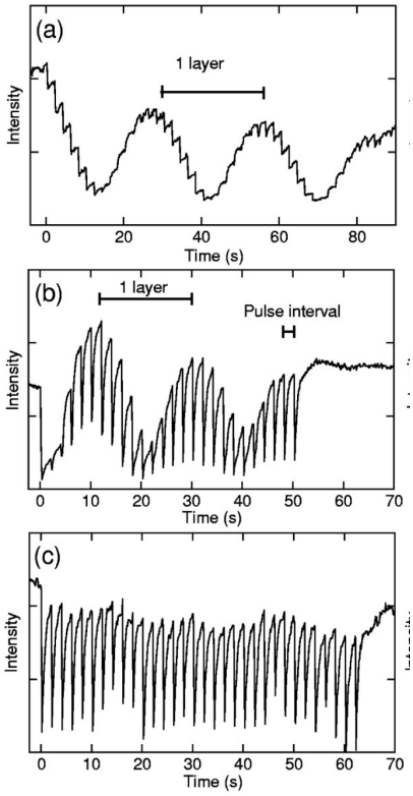

Figure 2.7: Comparison of RHEED oscillation behavior in layer-by-layer and step-flow growth modes.[30]

In order to interpret the RHEED specular intensity profiles, it is necessary to consider two points: the RHEED image formation mechanism and the crystal growth mechanism.

In an RHEED measurement an electron beam is directed at the surface of a crystal at grazing incidence, with an incident angle of less than about 5 degrees. The incident electrons can either be diffracted by periodic surface structures or reflected and scattered from the surface. The diffracted and reflected electron beams can be observed on a phosphor screen and imaged with a video camera, as shown in Fig. 2.2. For growth rate, growth mode, and coverage monitoring, the main interest is in the intensity of the specular reflection beam, since the reflected electron beam intensity is very sensitive to the surface roughness.

Nominally flat crystal surfaces generally have unit-cell steps due to the presence of a slight

miscut from an ideal high-symmetry direction. Additional steps may be present due to the nucleation of islands during thin film growth on flat surfaces. Such steps affect the RHEED image intensity and in this case, the image intensity is used to measure the variation of step edge density. Since the miscut angle does not change during growth, it is the density of island edges that is actually measured.

The presence of steps, either due to a crystal miscut or due to the presence of small islands, is an important factor in crystal growth. The increase of surface energy caused by the introduction of adatoms from vapor phase can be compensated either by nucleating islands or by incorporating adatoms into existing step edges. Step edges thus function as sinks for migrating adatoms on a surface. The average distance between step edges thus determines the maximum migration length for an adatom on the surface and therefore controls the kinetics of the growth process. The migration rate of adatoms is determined mostly by the surface temperature and to a lesser degree by other factors, such as the ambient oxygen pressure. The surface morphology of a crystal and the thin film growth mode is thus determined by the temperature, the average step distance on the surface, and the deposition rate, which for PLD is determine by the pulsed laser firing rate.[68]

Figs. 2.5 and 2.6 shows the relationship between the RHEED intensity time dependence and the surface state. The step flow growth mode (Fig. 2.5) dominates at high temperature and low pulse rates ($\leq$ 1 Hz).[30] When atoms are deposited on flat crystal surface under such conditions, (Fig. 2.5(b)), the RHEED intensity decrease suddenly due to an initial nucleation of islands on large terraces, which rapidly increases the step edge density. However, during the pulse interval, when no new atoms are deposited, surface migration of atoms quickly reduces the roughness, as atoms migrate and eventually find stable sticking sites at step edges (Fig. 2.5(c)). During this process, an approximately exponential RHEED specular intensity recovery can be observed.

As the temperature is reduced or the deposition rate increased, the layer-by-layer growth mode (Fig. 2.5) starts to dominate.[30] In this mode, when more atoms are deposited on a sample surface (Fig.2.5 (b)), the RHEED intensity decreases just like in the step-flow mode, because nucleation increases the surface roughness. At low temperature, the surface migration is slow, and therefore no recovery of surface flatness is observed. Flatness may only be recovered as a full unit cell layer is filled, recovering a flat surface and restoring a high specular RHEED spot intensity (Fig.2.6). For suitable growth rates, the RHEED intensity oscillates once for each monolayer of film growth. In this mode, the growth rate, expressed as the number of pulses required to grow 1 monolayer, can be easily calculated from the observed RHEED intensity oscillation period.

Fig.2.7 shows RHEED intensity data for a homoepitaial $SrTiO_3$ on $SrTiO_3$ growth experiment.[30] The growth conditions for each image are the following: laser pulse rate was 0.5 Hz, the growth temperature was (a) 780, (b) 1080, and (c) 1220°C. The layer-by-layer mode (a) disappeared and the step-flow mode (c) appeared at high temperature (Fig. 2.7).

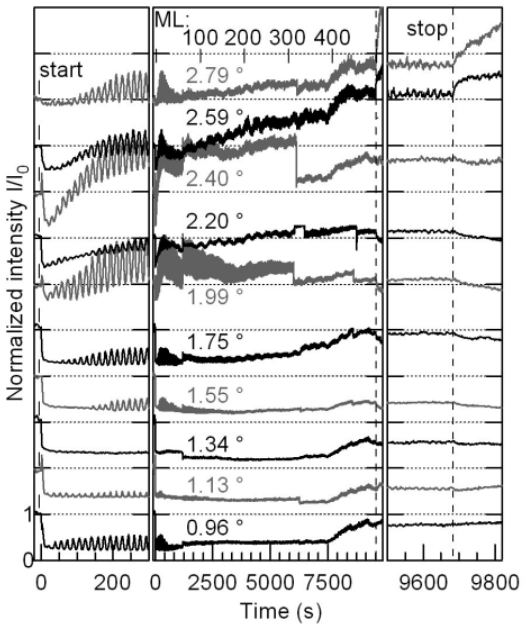

Figure 2.8: The effect of the incident angle on the RHEED intensity behavior.[65]

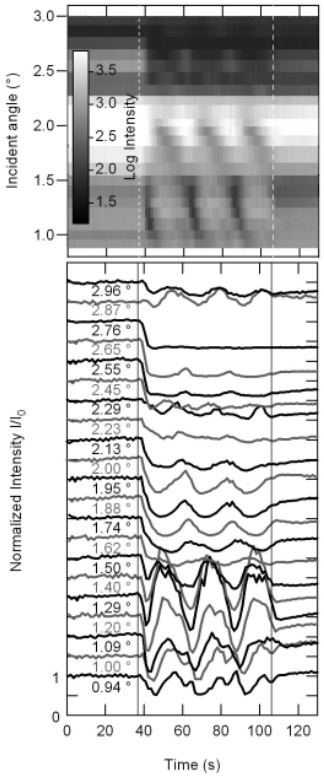

Figure 2.9: Change of RHEED oscillation phase with incident angle.[65]

While RHEED intensity oscillations offer very convenient tool for determining deposition rates during PLD film growth, it is not as easy to determine accurate fractional coverage during the initial stage of growth. One of the reasons for this is that while the oscillation period is a well-defined parameter, the oscillation phase can depend on the incident angle of the electron beam.[65] Due to this, it is not generally possible to use RHEED alone to determine the appropriate moment to stop deposition for an exactly filled unit cell layer, as this position does not correspond exactly to the intensity maximum of an RHEED oscillation (Fig.2.9 and Fig.2.8).[65] Due to this, incident angle optimization is needed, for example, with the help of a scanning-beam RHEED system, as was used in this work. In practice it is easy to measure

the distance between the specular spot and the direct beam on the RHEED phosphor screen and keep this distance constant in all experiments.

The particular RHEED system used in this study was equipped with double deflection coils (Fig.2.10),[65] allowing for the incident angle dependence to be measured in real time during film growth. It was thus possible to select the best incident angle data set after a deposition.

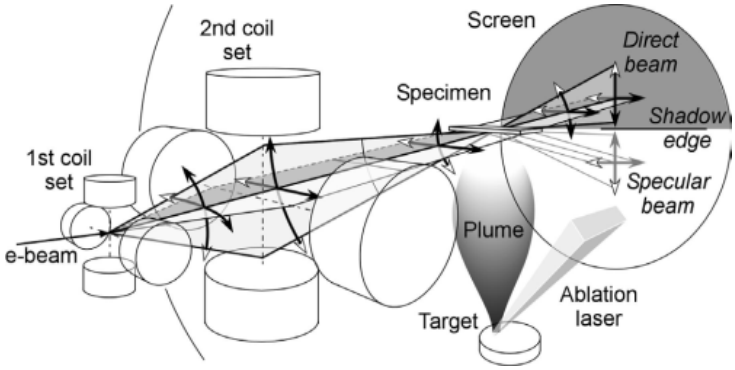

Figure 2.10: Scanning-beam RHEED system with two sets of electron beam deflection coil.[65]

2.2 Topography measurement

The topography measurement tools use in this work are all forms of Scanning Probe Microscopy (SPM), which is widely used for surface analysis. SPM is based on the use of a sharp tip that is scanned in a raster pattern over a surface, producing a height pattern that shows the real space local surface structure with very high spatial resolution. Depending on the type of tip and feedback mechanism, it is possible to measure atomic positions [6][37], local electronic states [8][37], local magnetism [53], conductivity [3][37][52][2][9], etc). These capabilities make SPM useful for thin film surface analysis in general but particularly valuable for the analysis of nanostructures, as in this work. A large body of literature is available on the various forms of SPM.[71, 70, 66, 69]

2.2.1 Atomic Force Microscopy (AFM)

Atomic Force Microscopy (AFM) is a form of SPM, where nanometer-scale surface features are imaged with a sharp tip attached to a flexible cantilever. The tip is subject to various contact forces when it is brought close to a surface, resulting in the deformation of the cantilever. In the most common form of AFM, the cantilever deflection, and thus the variation of the contact

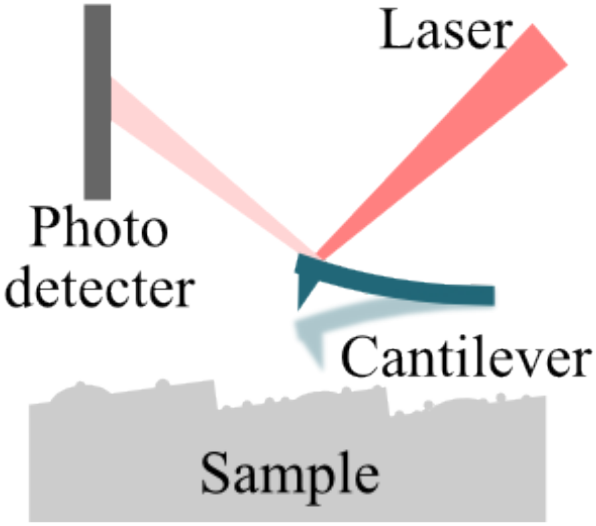

Figure 2.11: Illustration of an AFM system.

force, is measured optically. A laser beam is reflected from the cantilever and the reflected beam angle is detected with a position-sensitive detector. The position signal is used as a feedback parameter for a piezoelectric scanner, forming an image of the surface topography.

AFM is widely used in oxide thin film analysis, because the measurement of atomic force does not require a conducting sample, as is the case for scanning tunneling microscopy (Sec. 2.2.2). AFM can be used in air or vacuum, and even in a liquid. Although atomic resolution can be achieved [1], this is not usually possible due to the relatively large tip radius. Atomic resolution is not needed either for simple surface morphology analysis of thin film samples.

Fig.2.11 shows the essential features of an AFM system. A cantilever detects the force between the sample surface and the tip. A laser beam reflects from the back side of the cantilever and is directed at a photodetector. In this work, a four-segment detector was used that allows for independent detection of both vertical and lateral movement beam movement. Vertical movement is used to determine the local height information, while the lateral beam movement is used to measure the local friction force between a moving tip and the surface. The lateral forces give information about changes in the surface chemistry of a sample.

AFM can use many different detection modes, but the two basic techniques are known as the contact mode and the dynamic force mode. In contact mode, the cantilever is scanned over a surface while the tip touches the sample surface under a constant force. In dynamic force mode (DFM), the cantilever is vibrating with a small amplitude at a high frequency just

above the sample surface. Shifts in the vibration amplitude and phase can be used to measure distance (amplitude change) and surface composition changes (phase shift). Generally, the DFM mode is preferred, as it causes less damage to the surface and the tip than the contact mode measurements. A sample DFM image is shown in Fig. 2.11.

In this study, a SPM9600 (Shimadzu) microscope was used to measure the sample surface morphology. Both contact mode and DFM modes were used. The spatial resolution of this microscope was about 10 nm. Most of the images cover an area of 1000×1000 nm^2.

2.2.2 Scanning Tunneling Microscopy (STM)

Scanning Tunneling Microscopy (STM) [5] is another scanning probe technique, where the feedback signal is provided by a tunneling current flowing between the scanning tip and the sample surface. STM typically has higher spatial resolution, up to atomic scale, for well-ordered surfaces. Since the imaging signal is derived from a tunneling current, STM has the additional advantage that the local electronic structure of semiconducting samples can be probed in the same measurement as the topography. For example, the first real-space images of the Si 7×7 reconstruction were measured by STM.[6] STM is often used as a base for other SPM measurements, such as scanning tunneling spectroscopy (STS)[71]

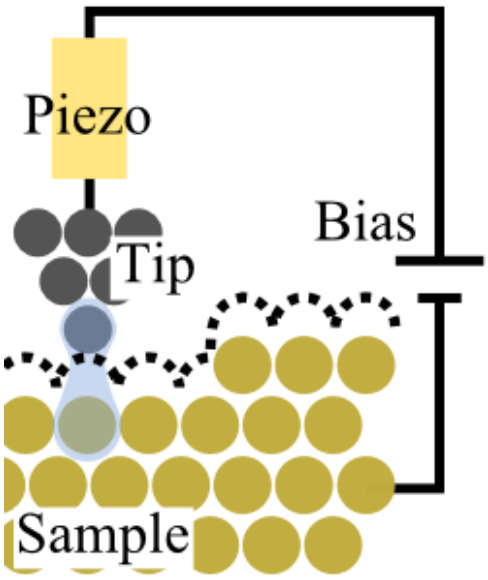

Figure 2.12: Illustration of the main parts of a scanning tunneling microscope.

Fig.2.12 shows a schematic diagram of a STM system. In STM, the distance between the tip and the sample is determined by measuring the tunneling current at a constant tip-sample

bias. The gap between the sample and the tip forms a barrier for electrons, which can still pass through the gap by tunneling. Since the tunneling probability depends exponentially on the gap width, it is possible to achieve very accurate height information. The main drawback of STM is the requirement of a conducting sample.

In the case of a metallic tip and sample, the tunneling current can be expressed as

$$I \propto \exp\left(-2\sqrt{\frac{2m}{\hbar^2}\left(\langle\phi\rangle - \frac{e|V|}{2}\right)}d\right) \tag{2.2}$$

where, ϕ is the average of work function of the two metals, d is the distance between the tip and the surface, m is the mass of an electron, e is charge of an electron, and V is the bias between the metals.

Because the tunneling current changes exponentially with distance, very small surface height changes can be detected. For example, under typical STM imaging conditions, the tunneling current changes by one order of magnitude for a distance change of 0.1 nm. Usually, a STM system has a feedback circuit that maintains a constant tip-to-sample distance with the help of a piezo element. In a constant current imaging mode the tip height is continuously adjusted by the feedback loop, keeping the tunneling current constant. The height information is derived from the piezo stage control voltage. The height resolution of a got STM system is on a pm order.

STM has two main parameter: **Bias** and **Current** because the current set-point determines the distance between the tip and the sample and the bias determines which electronic states are responsible for the tunneling current. By changing the bias, it is possible to image either the filled or the empty electronic states on semiconductor surface. For example, Fig. 2.13 shows $SrTiO_3$ topography images measure at different bias values.[58] These images cover the same area on a sample surface and have a scan size of 87×81 nm^2. The scan conditions are the following: Fig. 2.13(a) Sample bias (V_S)=+2.0 V, Tunneling current (I_t)=0.1 nA, Fig. 2.13(b) V_S=+1.0 V, I_t=0.1 nA, Fig. 2.13(c) V_S=+1.0 V, I_t=0.3 nA.[58]

In this study, an Omicron ultra-high vacuum STM/AFM scanner was used with a Matrix controller. All images were taken in the constant-current STM mode.

2.2.3 STM tip fabrication

In an ideal STM measurement, the tunneling current flows through a single atom at the end of the STM tip. In order to achieve the best spatial resolution and low-noise images, the STM tip needs to be sharp and clean. Tungsten STM tips are usually fabricated by electro-chemical etching of tungsten wire. Alloys of platinum and iridium are also commonly used [26], as

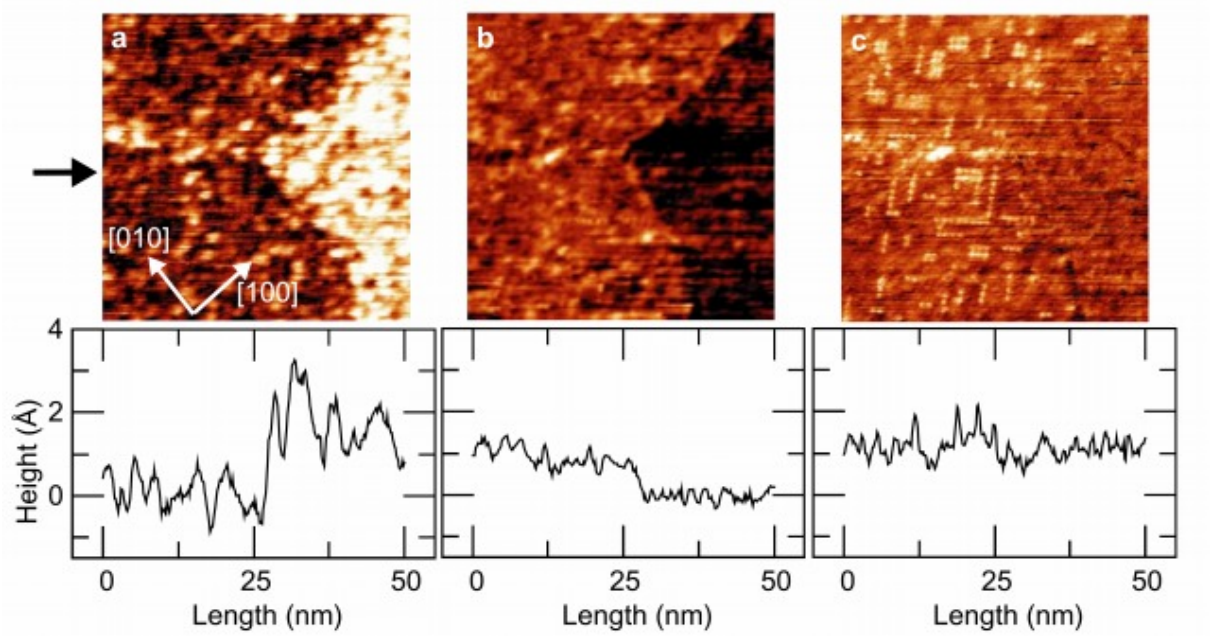

Figure 2.13: The effect of bias change on STM topography images[58]

is gold.[38] In this study, tungsten was used for STM tip material because tungsten tips are relatively easy to fabricate and can be used for a long time. The tip fabrication followed the process described by Lucier in a thesis.[32] After tip etching and mounting in the vacuum chamber, the tips were also annealed to remove the surface oxide layer.

Etching

Tip etching is a common technique of tip fabrication and has been reported by many authors.[13, 61, 14] Fig. 2.14 show the main components of the etching system used in this work. A tungsten wire was attached to one electrode and dipped into a potassium hydroxide electrolyte. Another ring-shaped counter-electrode was also dipped into the electrolyte. Bias was applied to the electrodes, resulting in the following chemical reaction [14]

$$anode: \quad 6H_2 + 6e^- \rightarrow 3H_2(g) + 6OH^- \tag{2.3}$$

$$cathode: \quad W(s) + 8OH^- \rightarrow WO_4^{2-} + 4H_2O + 6e^- \tag{2.4}$$

$$W(s) + 2OH^- + 2H_2O \rightarrow WO_4^{2-} + 3H_2(g) \tag{2.5}$$

The etching process occurred at the interface between the electrolyte and air (Fig. 2.15) until the wire is etched through and the bottom end of the tungsten wire drops off (Fig. 2.15(d)). This

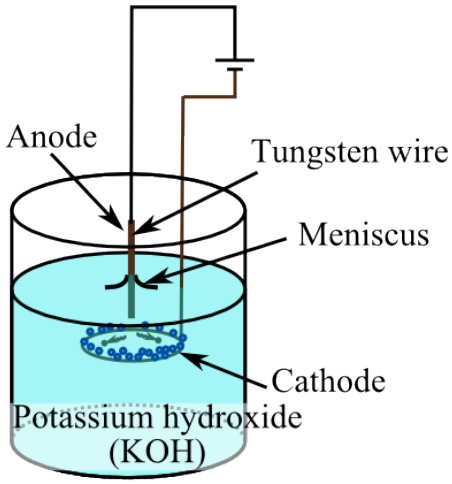

Figure 2.14: The STM tip etching system.

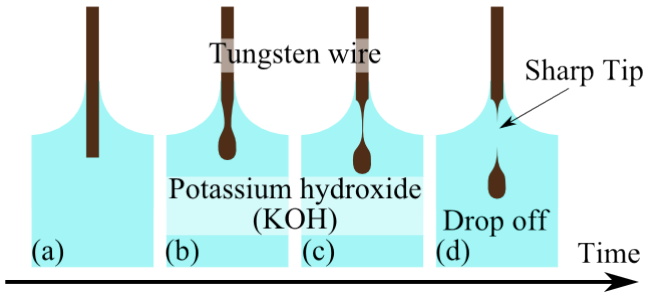

Figure 2.15: Illustration of the drop-off process of fabricating sharp STM tips.

is called the ”drop off” and the etching has to be stopped immediately after the drop-off occurs to prevent blunting the newly-formed sharp end.

Details of tip fabrication are discussed in Sec. 4.3.1.

Annealing

Annealing of tungsten tips is needed before imaging because in air, the tungsten wire is covered with a thin WO_3 layer immediately after etching. [10] [4] [12] Other contaminants may also be present due to the wet etching process.[50, 49, 7] The presence of an oxide layer has a negative effect on the image quality.[10] The formation of an oxide layer and the effects of vacuum annealing of tungsten tips has been studied by transmission electron microscopy. [10, 4, 12]

The tip annealing is done in the same UHV chamber that hold the STM, so that tips can be used immediately after annealing. At close to 1000 K, the following chemical reaction will occur

$$2WO_3 + W \rightarrow 3WO_2 \uparrow, \tag{2.6}$$

where WO_3 is reduced to WO_2, which is volatile and evaporates in high vacuum.

Laser heating was used to anneal the STM tips in the chamber. Laser light was brought into the chamber through an optical fiber and focused on the end of the tip. Although the tip temperature could not be accurately measured, the temperature of the back side of the tip

holder was measured instead and adjusted so that a clean tip was obtained. Detailed annealing conditions are explained in Sec. 4.3.2.

2.3 Transport measurement

The subject of this thesis is the analysis of the transport properties of nanodot arrays. The heterostructure samples were studied by measuring the temperature dependence of resistance in various geometries. Depending on sample resistance, either a 2-point (Sec. 2.3.1) or 4-point (Sec. 2.3.2) configuration was used. The 4-point method was used for low-resistance samples, where contact resistance can have a strong influence on the measurement result. For high-resistance samples, a simple two-point geometry was sufficient. The temperature was varied from room temperature to 4.2 K by dipping samples slowly into liquid He. The measurement limit for high-resistance samples was about $10^{10}\Omega$. The current-voltage (I-V) characteristics were also measured in order to confirm Ohmic conductivity and to determine an appropriate bias for the resistance measurements.

2.3.1 2-point probe method

The 2-point method is the most simple way to measure resistance. Since the measured resistance includes the contact resistance of the electrodes, it is only appropriate to use this technique for samples where the device resistance is much higher than the contact resistance. In this method, the applied bias is fixed and the current is measured. Since the dynamic range of current measurement is very high, from fA to mA, it is possible to reliably measure resistances of up to about $10^{12}\Omega$ (Fig.2.16), where various leak currents start to dominate and limit the measurement accuracy.

2.3.2 4-point probe method

The 4-point method is commonly used for measuring samples with moderately low resistances. In this geometry, 4 terminals are attached to a thin film sample in row. A constant current is fed through the sample from the outer electrodes, while the bias is measured between the inner two electrodes. The main advantage of this technique is the ability to eliminate the effects of contact resistance. However, current is not fed into high resistance sample (Fig.2.16).

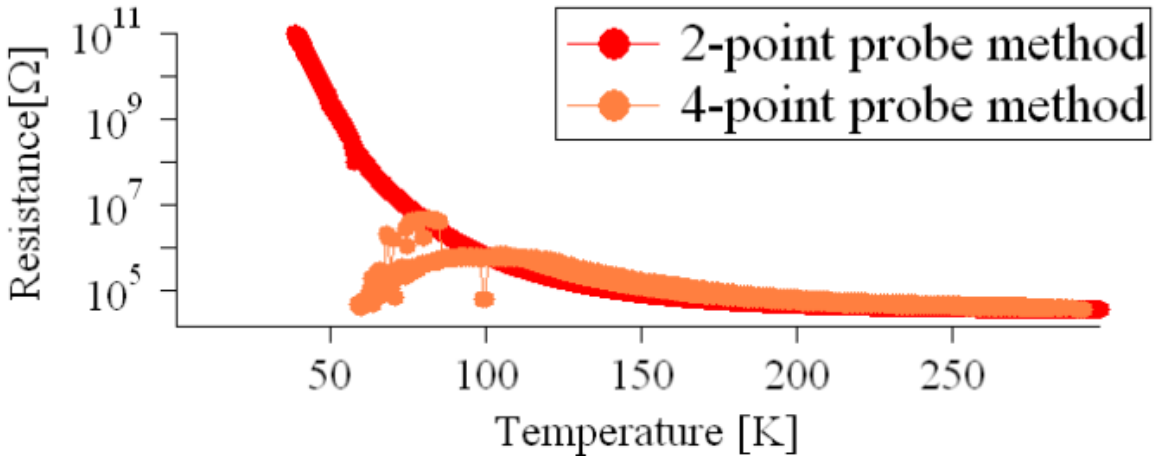

Figure 2.16: Comparison of 2-point and 4-point methods for the same sample.

2.4 Other equipment

2.4.1 Stylus profilometer (Dektak)

A stylus profilometer (Dektak) is a tool for measuring surface height variations. While STM and AFM are suitable for nm-scale measurements with excellent spatial resolution, it is difficult to measure large height variations over long distances, as is needed for film thickness calibration. For this purpose a stylus profilometer is used, which can measure long-distance scans over large surface features, such as shadow mask edges. Film thickness data from profilometry was used to check the deposition rate.

Chapter 3

Materials

The structure and basic electronic properties of materials used in this work are described in this Section. The starting point of the work is $SrTiO_3$ (Sec. 3.2), which is structurally a prototypical perovskite (Sec. 3.1), but has a number of unique electronic features that make it an exceptionally useful material for the construction of heterostructures. In this work, $SrTiO_3$ is combined with $LaTiO_3$ (Sec. 3.3), a nearly isostructural oxide with a different charge distribution.

3.1 Perovskite structure

3.1.1 structure

Both $SrTiO_3$ and $LaTiO_3$ have a perovskite structure, shown in Fig.3.1. The general chemical formula is ABO_3, where the *A*-site is usually occupied by a rare-earth atom or an alkali earth metal. The octahedrally-coordinated *B* site usually holds a transition metal atom. The anion is usually oxygen, although structures containing halogens, chalcogens or even pnictogens have also been reported. [67]

From a crystal structure point of view, a perovskite unit cell can be viewed as consisting of two atomic layers: AO and BO_2. Fig.3.1 and Fig.3.2 show the atomic layout in the AO and BO_2 layers. Ionic sizes shown in the Figures make it easier to see the positions of the cations. In reality, the largest atom in the unit cell is oxygen, and the perovskite lattice parameter varies little between different compositions, as it is the oxygen sublattice that mostly determines the ~ 0.4 nm lattice parameter. The similarity of lattice parameters for different perovskite compositions, together with the layered structure, make this material system suitable for the growth of various high-quality epitaxial heterostructures.

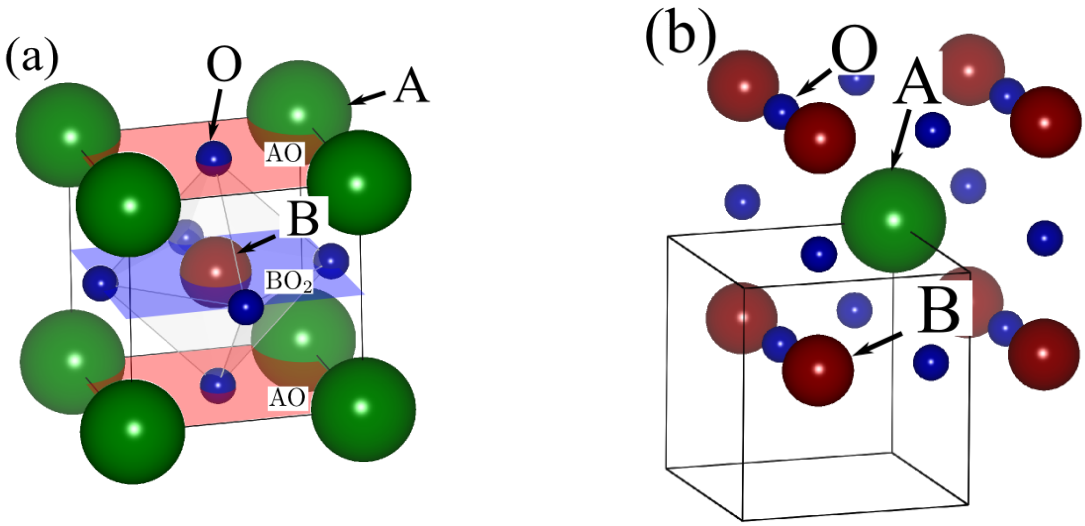

Figure 3.1: The ABO_3 perovskite oxide structure. (a) and (b) show two common ways of plotting the unit cell. The structure consists of layers of AO and BO_2.

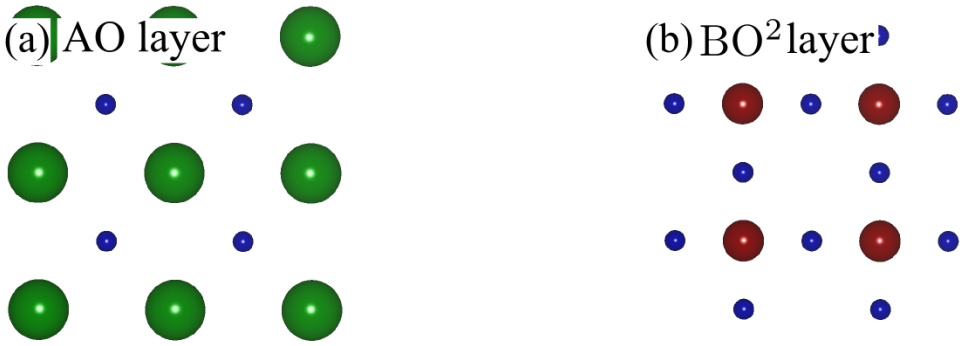

Figure 3.2: (a) AO and (b) BO_2 layers of the perovskite structure.

3.1.2 Physical properties

Since the perovskite structure is relatively insensitive to the particular cations at the *B*-site, it is possible to perform systematic studies as a function of the number of, for example, 3*d* electrons. One of the most common features transition-metal perovskites is the metal-insulator-transition. [15] Some of the phases appear as a function of the *d* level filling are illustrated for a 3*d* series of perovskites in Fig.3.3. For transition-metal ions that can support multiple valence states, the filling can be continuously adjusted by mixing divalent and trivalent cations at the *A*-site. One common example that is also relevant for this work, is the use of a $La_{1-x}Sr_xTiO_3$ compound, where x effectively determines the number of electrons in the Ti *d* level.[67] [11]

In addition to metal-insulator transitions, various other ordered phases can appear in structurally similar perovskites and related layered oxide compounds. Various forms of magnetic

order have been extensively studied, for example in manganites. While perovskites like $SrTiO_3$ can become superconducting at very low temperature, the best-known high-temperature superconductors, like $YBa_2Cu_3O_{7-\delta}$ is also based on the perovskite structure.

Ferroelectricity appears in various perovskites, with $BaTiO_3$ and $PbTiO_3$ being some of the well-known examples.[17] Ferroelectricity in these compounds is related to a change in the tolerance factor, or the lattice match between the natural lattice parameters of the AO and BO_2 layers. In $SrTiO_3$, the lattice match is nearly perfect, and $SrTiO_3$ remains paraelectric to the lowest temperatures. Substituting a larger ion, for example Ba, at the *A*-site can break this matching and created the asymmetry that is needed for ferroelectric order to exist.

Perovskite crystals can be easily grown in as thin films. Due to the relatively good lattice match of different perovskites, it is often possible to grow structuraly high-quality heterostructures with interesting new physical properties. For example, two dimensional quantum effects have been observed at $SrTiO_3$/Nb:$SrTiO_3$/$SrTiO_3$ interface.[22] $LaAlO_3$/$SrTiO_3$ heterostructures have been actively studied due to the metallic 2-dimensional system that appears at the interface between two insulators.[3]

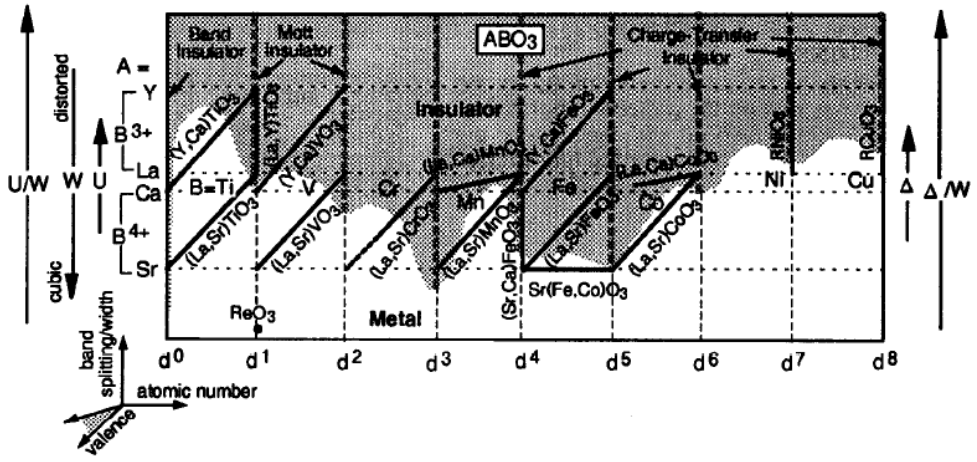

Figure 3.3: A summary of the various compositions that can be used to study the effects of band filling or band width on the metallicity of oxides.[11]

3.2 $SrTiO_3$

$SrTiO_3$ (STO) has a perovskite structure and is a band insulator. The valence band has the oxygen *p* character and is completely filled. The Ti *d*-band is empty but forms the conduction

band if $SrTiO_3$ is doped. The band gap is 3.2 eV, but the Fermi level is usually within a few hundred meV of the conduction band bottom.[39] The lattice constant is 3.905 .[48, 33]

Large $SrTiO_3$ single crystals can be grown by flame fusion, making $SrTiO_3$ a suitable substrate material for perovskite thin film growth. The surface of the $SrTiO_3$ (001) substrates used in this work was etched by buffered HF (BHF) [19] to obtain an atomically flat step-and-terrace crystal surface. A final, thermally stable surface can be obtained by annealing the substrates at a suitable temperature.[29]

The atomic structure of $SrTiO_3$ surfaces is still under debate. For heterostructure growth the reconstructions that occur on $SrTiO_3$ surfaces have little effect, but a number of different structures have been observed STM.[56, 57, 23, 16, 54] Some of the reconstructions that can appear on an annealed $SrTiO_3$ surface are illustrated in Fig.3.4.[57] Usually, however, the surface are not atomically ordered and, as in this work, the main interest is in the step edge morphology, rather than achieving atomic surface order.

$SrTiO_3$ can be doped to a metallic state in a number of ways. Partly due to the very high permittivity of $SrTiO_3$, the doping levels needed to induce a metallic state is exceptionally low, on the order of 10^{18} cm^{-3}. The most common dopants are substitutional Nb on the Ti site,[22], La dopant at the Sr site,[62] and oxygen vacancies.[18]

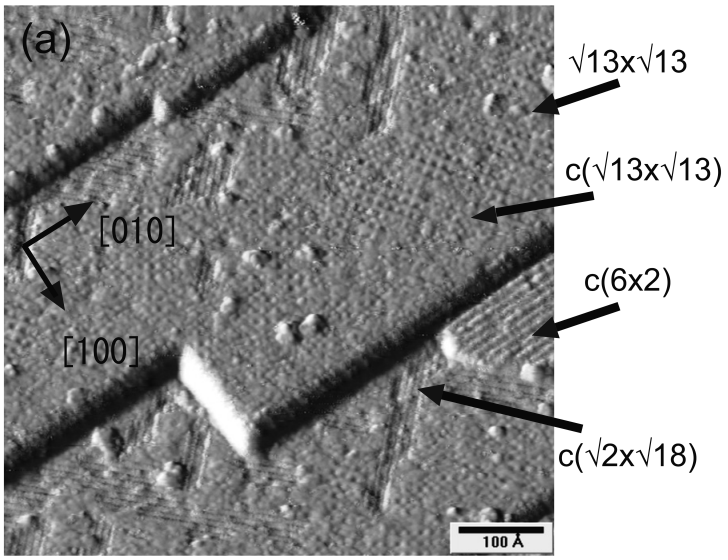

Figure 3.4: STM image of a $SrTiO_3$ surface showing several reconstructions. Imaging conditions: sample bias 1 V, tunneling current 500 pA.[57]

3.3 $LaTiO_3$

$LaTiO_3$ has a perovskite structure and despite having a single electron in the Ti *d* levels, the material is not metallic, but instead a Mott-Hubbard insulator.[47, 27, 62] In a Mott-Hubbard insulator the *d*-band is split due to electron correlations. [67] The insulating state can be easily broken by changes in the oxygen content.[27, 60]

In this work, $LaTiO_3$ is combined with $SrTiO_3$, since this offers a way to place a single LaO^+ atomic layer with a positive charge in the $SrTiO_3$ crystal. It thus crests a form of delta-doping, where the physical dopants are physically confined. The electronic width of such a heterostructure can, however, be much larger. A study of the spatial distribution of charge in $SrTiO_3/LaTiO_3$ heterostructures is the main topic of this work.

Chapter 4

Experimental conditions

4.1 Sample fabrication

The detailed experimental conditions used in sample fabrication by PLD are discussed in this Section. There are two basic type of nanostructure samples used in this study: the transport measurement samples (*Transport sample*) and sample used for topography analysis (*Topography sample*). The reasons for having to prepare separate, but equivalent samples for the two measurement types are explained in Sec. 4.1.4. The fabrication process is covered in Sec. 4.1.1, Sec. 4.1.2, and Sec. 4.1.3

4.1.1 Substrate

All thin film sample are grown on 0.2° miscut $SrTiO_3$ (001) single crystal substrates from Shinkosha. The reason for using miscut substrates was to obtain a surface with a regular step-and-terrace surface morphology and nearly equal terrace widths. On average, the step terrace width of a 0.2° miscut substrate with a cubic lattice parameter of 0.4 nm is $0.4nm/\tan(0.2^\circ) \simeq$ 110 nm. The substrates are chemically etched by buffered HF (BHF). The etching process is needed for obtaining flat terraces [19] Another advantage of etching is that it affects the surface stoichiometry. Since the HF etchant preferentially removes Sr from the surface, the etching no only produces a step-and-terrace surface, but also eliminates Sr from the surface.[19] 0.05 wt% Nb-doped $SrTiO_3$ substrates were also used for *Topography sample*, since these substrates are conducting and therefore suitable for STM experiments.

4.1.2 Substrate annealing

All samples were annealed before deposition. The as-received etched and polished $SrTiO_3$ surfaces are not stable at high temperatures. It is therefore necessary to recrystallize the substrate surface layer to form a stable step and terrace substrate. Flat terraces are necessary for the nanodot array fabrication, while regular terrace widths are important for maintaining a constant average diffusion length for adatoms deposted on the substrate surface.

The substrate pre-annealing conditions are shown in Fig.4.1. The substrates were heated to 1000°C, kept at this temperature for 10 minutes and cooled to the desired nanostructure fabrication temperature between 500 and 900°C. The oxygen pressure was 10^{-5} Torr during the annealing and the heating rate was 100 to 150°C/min. These conditions are similar to those suggested by Shimizu.[56] Although the annealing treatment reported by Shimizu et al. [56] was rather more complicated, just part of this condition is used for this study because it was not necessary to produce a particular $SrTiO_3$ surface reconstruction before the nanostructure growth.

High-temperature treatment of $SrTiO_3$ crystals always results in a certain level of Sr segregation to the surface. For the commercial substrates used in this work, the surface composition change starts at around 300°C [42] and it is thus unavoidable when the crystal growth has to be done at much higher temperatures. Although the surface is thus not ”atomically” flat [43, 56], it does not prevent the formation of the step-and-terrace surface and still allows the growth of perovskite nanodots on the flat terraces. The effects of annealing can be observed by AFM (Figs. 4.2 and 4.3). The as-supplied substrate, (Fig. 4.2) even after the chemical etching, has meandering step edges and atomically rough terraces. However, an annealed substrate (Fig.4.3) has straight step edges with constant single unit cell height and flat terraces.

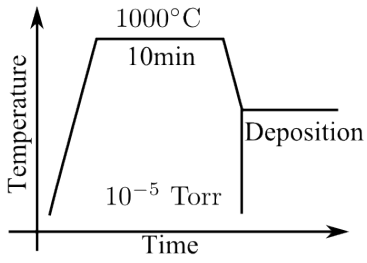

Figure 4.1: the $SrTiO_3$ substrate pre-annealing condition.

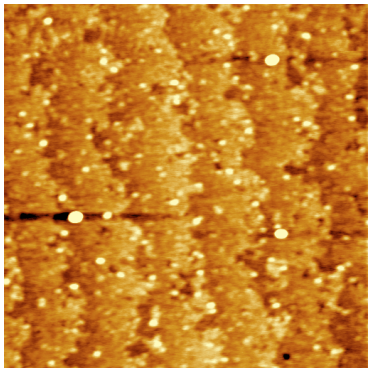

Figure 4.2: AFM image of the as-supplied $SrTiO_3$ substrate surface.

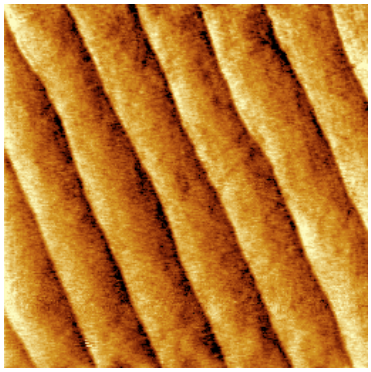

Figure 4.3: AFM image of an annealed $SrTiO_3$ substrate surface.

4.1.3 Growth conditions

$LaTiO_3$ deposition

The $LaTiO_3$ nanostructures were grown from a sintered $La_2Ti_2O_7$ target This phase is stable in atmospheric conditions and therefore convenient for use as an ablation target. The desired $LaTiO_3$ phase can be obtained during growth by a suitable selection of the ambient oxygen pressure.

The phase that forms during $LaTiO_x$ film growth under different oxygen pressures and temperatures has been carefully studied and the data can be found in the literature (Fig.4.4). [45] Because the $LaTiO_3$ perovskite phase was desired for this experiment, and the published data shows the formation of the $La_2Ti_2O_7$ phase at oxygen pressures above 10^{-4} Torr, [45] relatively weakly oxidizing conditions were selected for the experiments, with the oxygen pressure set at 10^{-6} Torr. The base pressure of the PLD chamber was $\sim 10^{-8}$ Torr. Similar growth conditions have been used before for thicker $LaTiO_3$ film growth.[55, 36, 46]

The excimer laser pulse rate was 2 Hz. The ablation pulse energy was 18.3 mJ with an ablation spot size of 1.94 mm^2, giving a laser fluence of ~ 0.9 J/cm^2. The deposition rate was estimated from ~ 100 nm-thick films deposited at 700°C. A thickness calibration sample was made for each PLD machine run cycle in order to guarantee accurate rate measurement. During the initial stage of thick film growth, real-time RHEED oscillations were also recorder and the deposition rate from the RHEED oscillation time period was cross-checked against the thickness obtained from later profilometer scans. Fig. 4.6 shows one typical example. The deposition rate from the sample shown in Fig. 4.6 was estimated as 53 pulses/uc (uc=unit cell). The fractional surface coverage during the actual nanodot array fabrication was calculated from this deposition rate. The growth temperature and the laser ablation pulse count (coverage) were varied in order to fabricate nanodot arrays with various average dot sizes and nanodot coverages.

$SrTiO_3$ deposition

A capping layer of $SrTiO_3$ was needed for the *Transport sample* for two main reasons, in order to protect the nanodot array during thermal treatments and to avoid problems associated with surface depletion layers in the transport measurements. It is well known that oxygen vacancies are formed in the substrate surface during the pre-annealing treatment and that films grown by PLD are usually not fully oxidized during growth. Since oxygen vacancies work as dopants in $SrTiO_3$, on average donating two electrons for each missing oxygen, it would be difficult to interpret the transport behavior of nanodot samples that also contain oxygen vacancies.[18] To eliminate oxygen vacancies in $SrTiO_3$, all *Transport sample* were annealed (post anneal) in air

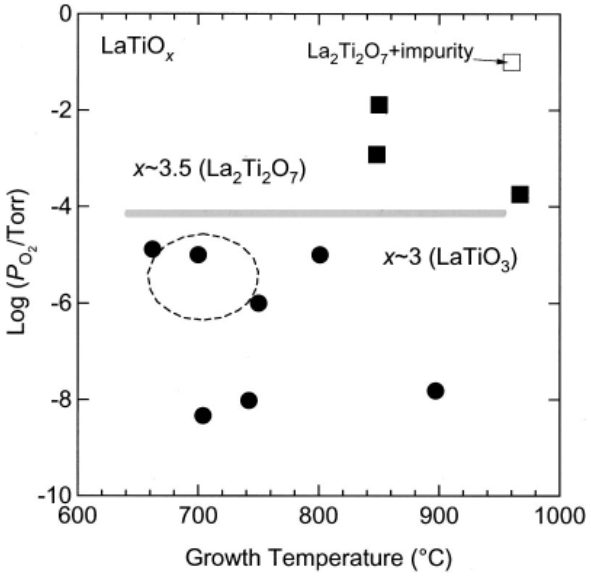

Figure 4.4: Phase diagram for $LaTiO_x$ film growth under different oxygen pressures. [45]

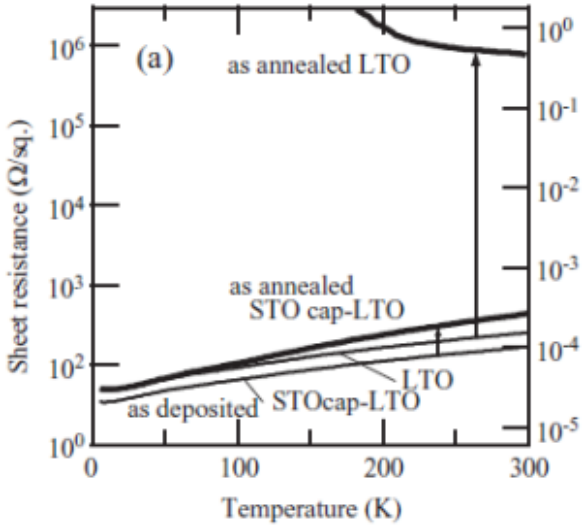

Figure 4.5: Degradation of $LaTiO_3$ by annealing.

at 400°C for 6 hours.[46] However, it has also been reported that the $LaTiO_3/SrTiO_3$ transport properties changed by post annealing.[36] This may be caused by two reasons: the formation of the $La_2Ti_2O_3$ phase in thick films and the appearance of a deep surface depletion layer.[45] The $SrTiO_3$ cap that was deposited after the $LaTiO_3$ nanodot array can prevent both problems (Fig.4.5).[36] Obviously, the capping layer was deposited only on the *Transport sample*.

The $SrTiO_3$ deposition conditions were almost the same as those used for the $LaTiO_3$ nanodot growth.

The excimer laser pulse rate was 2 Hz. The ablation fluence was estimated as 18.3 mJ / 1.94 mm^2, giving $\sim$ 0.9 J/cm^2. The deposition rate cross checking by profilometry was done wit thick films ($\sim$ 200 nm), deposited at 500°C during every machine time, while also counting RHEED oscillation peaks. Fig. 4.7 shows one of the examples of $SrTiO_3$ growth. The deposition rate estimated from Fig. 4.7 was 27.5 pulses/uc. The capping layer thickness was fixed at 20 uc. The growth temperature was fixed at 500°C, which was intentionally quite low for $SrTiO_3$. This choice was made for two reasons. The $LaTiO_3$ nanodot size depends on temperature and time after deposition. If a nanodot temperature is kept at high temperature for a long period, the average dot size will increase due to surface diffusion. It is thus preferable to quickly cool the sample to a lower temperature, where surface migration stops, before growing the capping layer. If this were not done, the *Topography sample* and *Transport sample* could be systematically different, depending on whether a cap layer is grown or not. Secondly, the

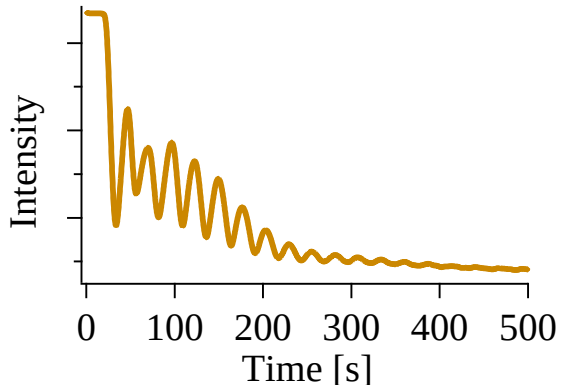

Figure 4.6: Specular RHEED intensity oscillations during $LaTiO_3$ deposition. Each oscillation corresponds to the growth of a single perovskite unit.

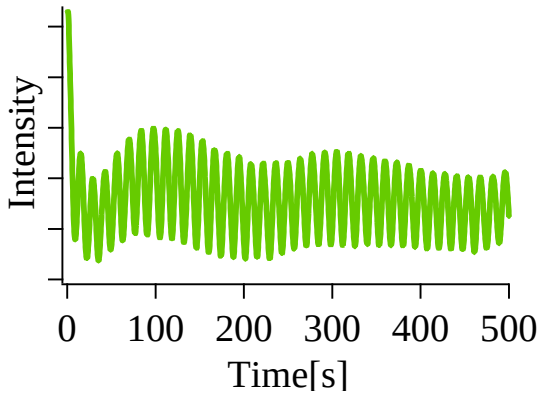

Figure 4.7: RHEED intensity oscillations during $SrTiO_3$ cap layer growth.[36]

purpose is to observe the transport behavior in the $SrTiO_3$ substrate, under the nanodots. It is known that the carrier mobility in $SrTiO_3$ is a strong function of crystalline. Growing the cap layer at a low temperature therefore gives ensures that the cap layer contribution to the transport properties of a nanodot array are minimized, while maintaining a dielectrically continuous system. A change in the transport behavior can be seen when the cap layer is grown at very high temperature (Fig.4.8).

The $LaTiO_3$ and $SrTiO_3$ deposition conditions are summarized in Table 4.1.

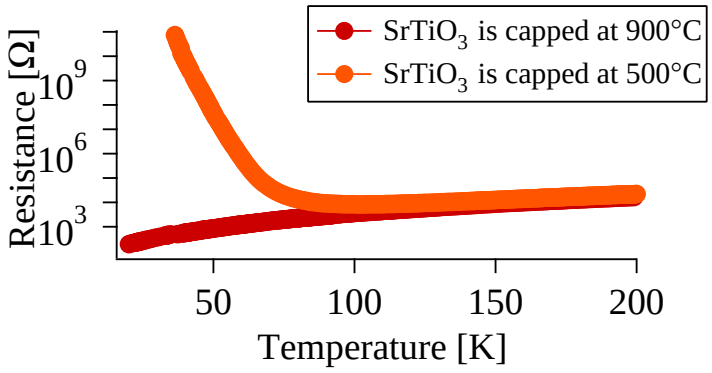

Figure 4.8: The effect of elevated cap layer growth temperature on the transport properties of a heterostructure.

Table 4.1: Summary of the deposition conditions.

Target	Pulse rate [Hz]	Laser fluence $[J/cm^2]$	Oxygen pressure [Torr]
$LaTiO_3$	2	$18.3mJ/1.94mm^2 \simeq 0.9$	10^{-6}
$SrTiO_3$	2	$18.3mJ/1.94mm^2 \simeq 0.9$	10^{-6}

Target	Deposition rate [pulses/uc]	Deposition temperature
$LaTiO_3$	53.0	Depends on sample
$SrTiO_3$	27.5	500°C

4.1.4 Sample structure

Two kinds of samples were fabricated for *Transport sample* and *Topography sample*. The structures of *Transport sample* and *Topography sample* are compared in this Section.

The basic methodology of the experiments are based on the idea of comparing the statistical morphology parameters of a nanodot array with the transport behavior. Unfortunately, in order to determine the nanodot morphology, the nanodots need to be on the sample surface and accessible to AFM or STM. For transport measurements, the nanodot arrays need to be capped, making it impossible to observe the shapes and sizes of the nanodots. Pairs of samples therefore need to be made, with and without the capping layer. Ideally, the $LaTiO_3$ deposition and annealing conditions should be exactly the same for both *Transport sample* and *Topography sample* in order to make reliable comparisons of the topography and transport results. However, it is difficult to obtain good repeatability over long term in PLD growth experiments. The process variations are caused by limited control over various instrument parameters, such as the excimer laser gas aging, heating efficiency variations, or the gradual loss of vacuum chamber viewport transparency due to the accumulation of ablated material in the chamber. The *Transport sample* and *Topography sample* pairs were fabricated separately, but always during the same machine run to keep the instrumental variations as small as possible and samples with the same nominal $LaTiO_3$ growth parameters were fabricated one after another under the same annealing and growth conditions.

Transport sample

The *Transport sample* was used for transport measurement to understand which nanodot coverage is critical for metallic conductivity to appear in a nanodot array. The main distinguishing features of the transport samples was the growth of the $SrTiO_3$ capping layer and the use of insulating, on-doped $SrTiO_3$ substrates. The $LaTiO_3$ growth conditions were the same as for a companion *Topography sample*. After deposition, the *Transport sample* was post-annealed at 400°C for 6 hours in air to fill oxygen vacancies, as was explained in Sec. 4.1.3. The *Transport sample* thus had a structure of $SrTiO_3/LaTiO_3/SrTiO_3$, as illustrated in a cross-section diagram in Fig. 4.9. The resistance of the *Transport sample* was measured as a function of temperature by a simple 2-point probe method between wire-bonded points on the sample surface.

Topography sample

The *Topography sample* growth was done on 0.05 wt% $Nb:SrTiO_3$ substrates that are conductive (Sec. 4.1.1) as required for STM samples. The requirements and details of the STM work can be found in Sec. 2.2.2.

The $LaTiO_3$ nanodot arrays were not capped or annealed after growth, as the presence of oxygen vacancies, either in the substrate or in the dot structures, does not affect the surface morphology of the nanodot arrays. STM and AFM were used to measure the average nanodot sizes, nanodot distances, to calibrate the coverage, and also monitor the evolution of the dot shapes. The sample structure is illustrated in Fig.4.10.

Table. 4.2 summarizes the differences between the *Transport sample* and *Topography sample* structures.

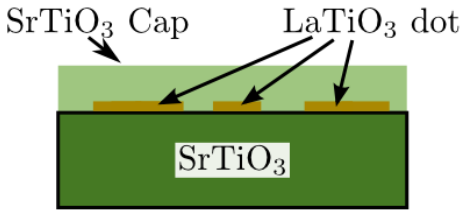

Figure 4.9: Structure of a transport characterization sample.

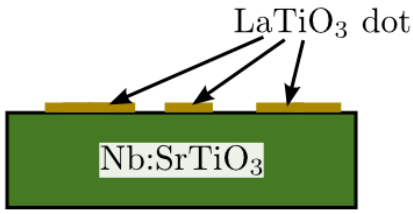

Figure 4.10: Structure of a nanodot array sample used for topography measurements.

4.1.5 RHEED incident angle

Electron diffraction monitoring is a common technique for determining growth rates in PLD experiments. However, in most published works, the incident angle of the RHEED beam is not

Table 4.2: Two sample difference

Sample	Substrate	$LaTiO_3$ deposition
Transport sample	Non-doped $SrTiO_3$	same as *Topography sample*
Topography sample	Nb doped $SrTiO_3$	same as *Transport sample*

Sample	Cap	Post anneal
Transport sample	$SrTiO_3$ Cap(20uc)	400°C 6 hour in air
Topography sample	No cap	Needless

specified and often not well controlled. Since in this case, repeatability between experiments was very important, special care was taken to maintain an optimal incident angle for the electron beam on the sample surface.

The RHEED incident angle was optimized by using the beam scanning option, where several diffraction patterns can be measured in a rapid succession, each for a different incident angle of the electron beam. An RHEED electron gun with two sets of beam deflection coils was used for this purpose, as explained Sec. 2.1.3. Figs. 4.11 and 4.12 show RHEED intensity oscillations measured at different incident angles during $LaTiO_3$ deposition at 700°C under 10^{-6} Torr of oxygen. From this data, it is clear that an incident angle of 1.4° to 1.5° is the best for observing coverage-dependent oscillations in RHEED intensity, consistent with earlier published results shown in Fig.2.9.[65]

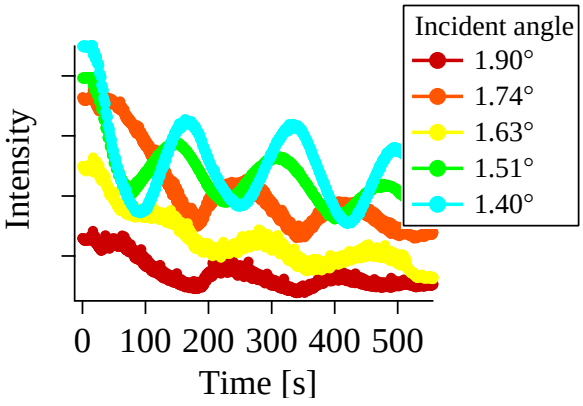

Figure 4.11: RHEED specular intensity incident angle dependence.

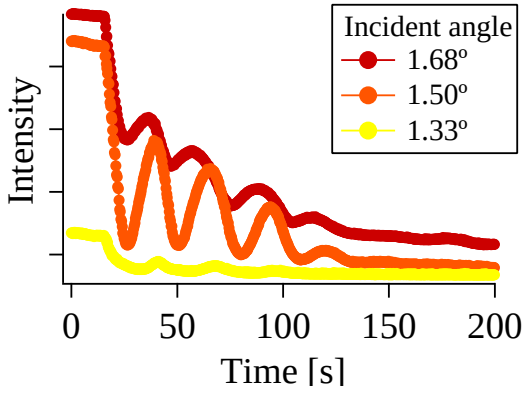

Figure 4.12: RHEED intensity angle dependence

4.1.6 SiC emissivity

SiC was used as a heat absorber material in the laser-heated high-temperature sample holders because SiC has a nearly constant emissivity and stable at high temperatures. The emissivity is important in this experiment because the temperature of the head absorber block is measured with an optical pyrometer. The sample temperature, on the other hand, is the most critical parameter for PLD film growth.

The emissivity of the sample holder heat absorber block was calibrated against a simultaneously temperature measurement with a standard K-type thermocouple under vacuum (10^{-3} Torr). The data analysis was based on the Stefan-Boltzmann law (Eq. 2.1).

Figs. 4.13 and 4.14 show the measurement results. The vertical axes ares the heating laser power that is incident on the SiC block. The horizontal axis shows the fourth power of temperature (T^4) which is measured by the pyrometer under different emissivity settings and the data is compared with the thermocouple(TC) temperature. Due to the saturation of the pyrometer reading, the $\varepsilon = 0.1$, 0.2 in Fig. 4.13 show temperature saturation at $T^4 \sim 8.6 \times 10^{12}$ ($T = 1441^{\circ}$C). The power is linear to T^4. This indicates that almost all of the heating laser power is lost by thermal radiation and conductive heat losses through the sample holder body are minimal. This reflects the good heat isolation of the sapphire ball mounting geometry that only makes point contact at three points with the SiC block. Because the heating power proportional to T^4, the following equation can be applied

$$P = A\varepsilon T^4 \tag{4.1}$$

$$P/T^4 = A\varepsilon \tag{4.2}$$

Here, A is a constant value including the Stefan-Boltzmann constant and the optical losses in the vacuum chamber viewports in front of pyrometer, and P is the diode laser power. The constant A can calculated from Fig. 4.14, which shows a P/T^4 vs ε plot. The optimal emissivity setting for this instrument can deduced from A and the P/T_{TC}^4 plot, marked by the green point in Fig. 4.14. The emissivity calculated from this data was 0.726. However, the emissivity during film growth in the PLD chamber may be slightly lower than this value because during film growth in the PLD chamber, an additional protective quartz or sapphire plate is in front of the viewport used to observe the sample holder temperature. The effective emissivity for the PLD chamber was calculated by considering the PLD constant $A_{PLD} = P/T^4\varepsilon$. The true effective emissivity ε_{eff} can be calculated in the following way by considering the known relation between power and temperature.

$$P/T^4 = A \cdot 0.762 = A_{PLD} \cdot \varepsilon_{eff} \tag{4.3}$$

$$\varepsilon_{eff} = \frac{A \cdot 0.762}{A_{PLD}} \tag{4.4}$$

Te effective emissivity for a SiC block in the PLD chamber was calculated as 0.674.

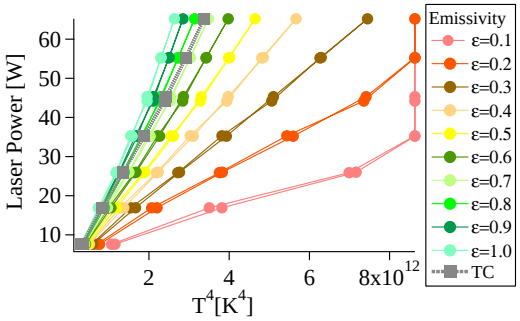

Figure 4.13: Sample heating laser power vs the fourth power of temperature.

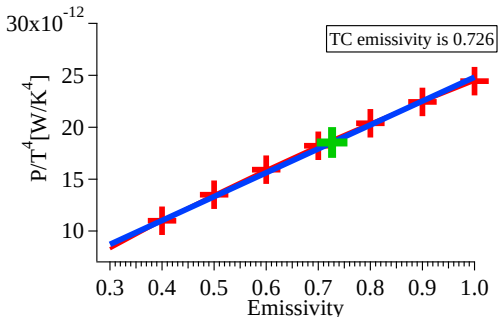

Figure 4.14: Power/the fourth power of temperature vs emissivity.

4.2 Transport measurement

The resistivity of thin film samples was measured in either 2-point or 4-point geometries, depending on the resistance range. (Sec. 2.3.1, Sec. 2.3.2).

Electric contact to the capped nanodot array samples was made by ultrasonic wire bonding directly to the sample surface. The bonding wedge applies enough force to the surface of the crystal to generate microcracking to a depth of several micrometers under the aluminum wire bond point. The bonding wires can thus make contact to the buried metallic layer without the need for special patterning techniques. Aluminum wires form an Ohmic contact with doped $SrTiO_3$ samples.

The current flow direction is important for transport measurement in this work because the transport properties may be anisotropic due to the presence of surface steps. Very large anisotropy can be observed in samples containing metallic nanowires. [35] All $SrTiO_3$ substrates used in this work were atomically flat and had a regular step-and-terrace structure (Sec. 4.1.1). The substrates also had a relatively narrow terrace width, which makes it easier to obtain regular surfaces during a short high-temperature pre-annealing process. However, the narrow terraces also mean that it is relatively easy to form $LaTiO_3$ wire structures along the step edges due to

the step flow growth mode (Sec. 2.1.3). Since the interface conductivity along the wire direction is much higher than between isolated nanodots, transport measurements would become unreliable. To avoid such problems, resistance was always measured in two direction, as explained in Fig. 4.15. Technically this was easy to achieve, since the step direction was known from the AFM images and wires could be bonded to the crystal surface so that the current flow in the resistance measurements was either parallel or perpendicular to the steps.Most of the resistance data used in this work was obtained in the perpendicular measurement direction.

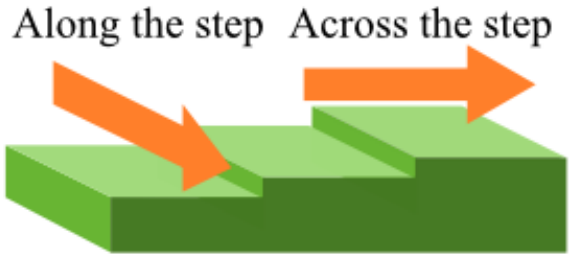

Figure 4.15: Definition of the current flow directions as used in the transport measurements.

4.3 STM preparation

4.3.1 Tip etching

Atomically sharp and clean tips are required for stable STM imaging. Electrochemical etching is the most common process for fabrication sharp tungsten tips, as explained in Sec. 2.2.3. KOH is the usual electrolyte for tungsten wire etching.[49, 50, 25] The etchant solution concentration was 1 mol/l and the etching was done at a constant 3 V bias. The tungsten wire diameter was 0.3 mm. The etching current was measured with a transconductance amplifier and digitized with the help of a LabVIEW program on a computer. Various electrode configurations can be used in the etching process,[14, 25, 34, 51, 12] but the precise cathode layout is not critical for the etching of a sharp tip. In this case, the cathode electrode was a square-shaped wire loop, placed along the outer edge of cuvette and dipped approximately 2 mm below the electrolyte surface. The shape of the meniscus forming around a tungsten wire in the center of the etching solution is quite important for obtaining a sharp tip shape. The meniscus is the area where the liquid surface is lifted by surface tension on the surface of the tungsten wire, shown in Fig. 2.14. While etching, the wire diameter changes and the meniscus may drop during etching. If the meniscus drops, etching would continue only in the middle point of the tip and the tip

shape will usually become irregular. A typical tip that appears if the meniscus is allowed to drop is shown in Fig. 4.16. To prevent this problem, the bias applied to the tip was cut immediately if the meniscus dropped. This allowed for manual readjustment of the wire position. The meniscus shape is also important because it affects the tip sharpness and symmetry.[32] The bias applied to the tip needed to be stopped quickly after the bottom part of the wire has dropped off (Sec. 2.2.3) or else the sharp end of the tip would continue to be etched and becomes blunt.[51, 14, 63] At the final stages of etching, pulsed bias was used instead of a constant voltage. By periodically applying a small negative bias on the tip and measuring the circuit current, it was possible to determine automatically when a drop-off event had occurred. The quality of the tip shape was judged with an optical microscope. If tip is sharp enough, the sharp end of the tip cannot be focused on by an optical microscope, as the tip diameter is on the nm scale. This is an easy way to quickly check the sharpness of an etched tip. Fig. 4.17 illustrates an example of a good and sharp tungsten tip.

Figure 4.16: Badly etched dull tip.

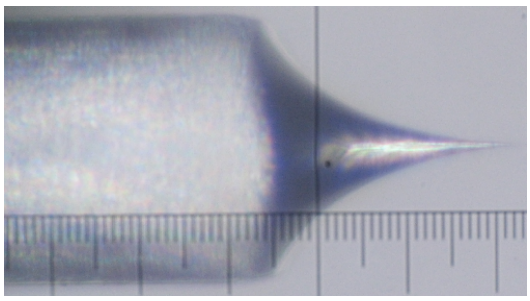

Figure 4.17: Well-etched sharp tungsten tip.

4.3.2 Tip annealing

The tungsten tips formed by etching quickly form a layer of oxide on the surface. If such tips are directly used in STM experiments, the resulting images tend to be unstable and noisy. Tip annealing is therefore needed for tungsten tips to remove the oxide layer. [10, 4] In this work, the etched tips were mounted on tip carriers used by the STM and placed in a special ceramic heating stage. This allowed the existing laser heating system, normally used for sample fabrication, to be used for tip annealing as well (Fig.4.18).[28] A focusing lens was placed in the tip stage to focus the heating laser light on the apex of the tip (Fig.4.19). The temperature of the sharp end of the tip can not be done by pyrometry, as the area is too small. Due to this, the temperature of the tip holder was measured from the backside. Although this temperature was different from the actual tip temperature, it only served as a reference for reproducible annealing

treatments. The annealing condition were: 800°C for 2 s and 400°C for 5 min in ultra-high vacuum. The 2-second annealing was for removing the oxide film from the tip by evaporating the WO_2 layer. Longer annealing would tend to make the tips blunt.[12, 32] The 400°C anneal was mostly needed to clean other contaminants from the tip wire and the tip carrier in order to maintain good vacuum conditions in the chamber. The effect of the tip annealing treatment can be seen in Figs. 4.20 and 4.21. The same sample was measured in both cases. The image size is 267×267 nm^2. It is clear that noise lines disappeared after tip annealing. This indicates that the oxide layer was removed from the tip by a brief high-temperature annealing treatment.[10]

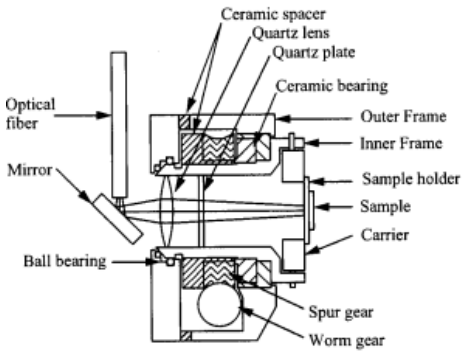

Figure 4.18: Annealing system of sample.[28]

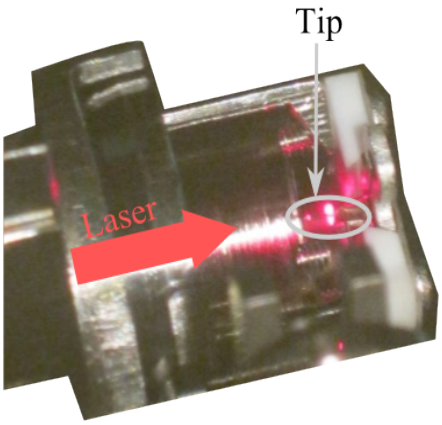

Figure 4.19: Annealing system of for STM tips.

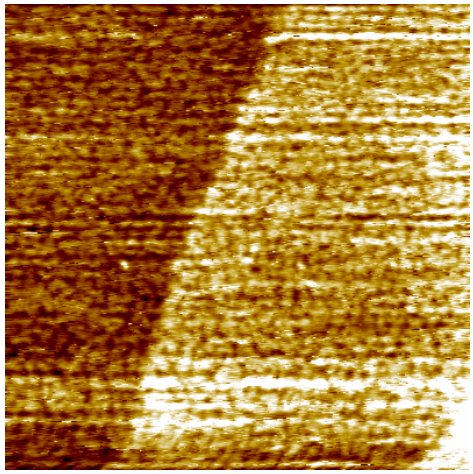

Figure 4.20: STM image taken with a tip before annealing.

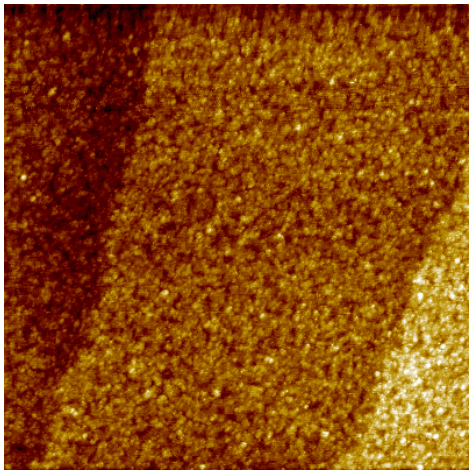

Figure 4.21: STM image taken with an annealed STM tip.

4.3.3 STM measurement conditions

Conducting Nb-doped(0.05wt%) substrates were used for the STM work as explained in Sec. 4.1.1. The nanodot array samples were fabricated in the PLD chamber and moved to the STM chamber (ex-situ). All samples were measured under 5×10^{-9} Torr vacuum. The tip bias and sample current varied, depending on sample.

Chapter 5

Results and discussion

There are two main methods that can be used to estimate the coverage of $LaTiO_3$ dots on a $SrTiO_3$ substrate: in-situ RHEED during film growth and ex-situ STM. To distinguish the two types of measurements, two different units are used in this Section. When deposited $LaTiO_3$ quantities are given in unit cells (uc), the number refers to a layer thickness estimate based on RHEED. Fractional-layer coverage values are reported in "%", based on STM data. When discussing the STM imaging conditions, V refers to the sample bias and I is the tunneling current.

5.1 Annealing temperature dependence of $LaTiO_3$ dot size

When analyzing the formation of a metallic conduction path through a fractional layer of nanodots, it is clear that the shape and size of the nanodots is important. The scale of the nanodots also dictates the use of certain experimental approaches. For example, large nanodots, on the scale of tens of nm can be easily detected by conventional AFM. Dots that are smaller than 10 nm, however, can not be easily distinguished, since this length scale is comparable to the radius of the AFM tip. In such cases, only STM offers a sufficient spatial resolution. It is well known that the morphology of the initial growth layer depends on the temperature. At very high deposition temperatures, the surface mobility of adatoms can be large enough for step-flow growth to occur. In this case small nanoscale dots on the crystal surface become unstable and adatoms quickly migrate to step edges on the surface, forming nanowires instead of nanodots. [31] Obviously, this is not optimal for the analysis of percolative conduction in nanodot arrays. Control over the average nanodot size is also important for determining which nanodot characteristics affect the formation of metallic conduction paths in oxide systems with lateral inhomogeneity.

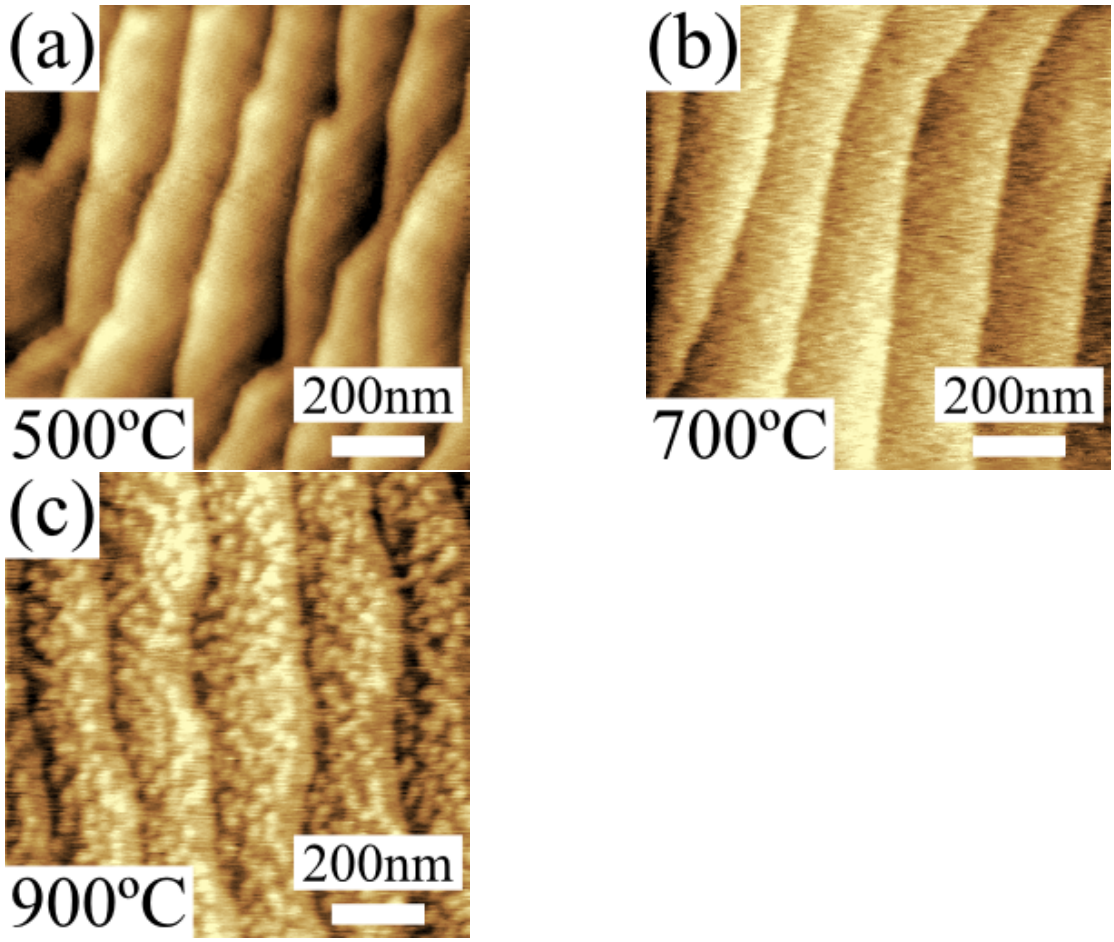

Figure 5.1: AFM images of fractional $LaTiO_3$ nanodot layers deposited at (a) 500°C, (b) 700°C, and (c) 900°C.

Temperature is the most important parameter controlling the nanodot size because it directly affect the adatom migration rate and, for a given time, length. Fig. 5.1 shows typical surface morphologies of fractional $LaTiO_3$ layers as measured by AFM. The coverage is 0.3 uc for all samples, as estimated from the RHEED oscillation period and laser pulse count, but the deposition temperatures are 500°C in (a), 700°C in (b), and 900°C in (c). The image size is 1000×1000 nm^2 in all three cases.

It is clear that at the lowest temperature, individual dots can not be resolved by AFM. This is also reasonable, because from earlier STM experiments it is known that at this growth temperature, the characteristic nanodot diameter tends to be less than 5 nm.

At the highest temperature of 900°C (Fig. 5.1(c)), a clear dot pattern can be seen. All dots have the same single unit cell height and the average dot diameter can be estimated from

this figure as 48 nm. For intermediate temperatures, it may be able to detect the presence of a nanodot array, but the AFM spatial resolution is not sufficient to perform useful statistical analysis of coverage or dot sizes.

Despite the limitations of the AFM measurement, it is clear that the average nanodot size does indeed depend on the growth temperature. Based on such initial AFM experiments, further work on $LaTiO_3$ nanodot growth focused on the 700 to 900°C temperature range, illustrated by Figs. 5.1(b) and (c).

5.2 900°C $LaTiO_3$ deposition

The 900°C growth temperature was the highest nanodot growth temperature, limited by the appearance of step flow and the formation of nanowires along the surface step edges. The surface coverage was varied to determine the critical coverage where metallic conductivity appears. At this growth temperature, the nanodots are large enough to be imaged by AFM, which showed that the dot height is always equal to 1 uc (Fig.5.1). The large $LaTiO_3$ dots can also be conveniently image by STM. A summary of the 900°C sample is in Sec. 5.2.3.

5.2.1 Transport property

Coverage dependence

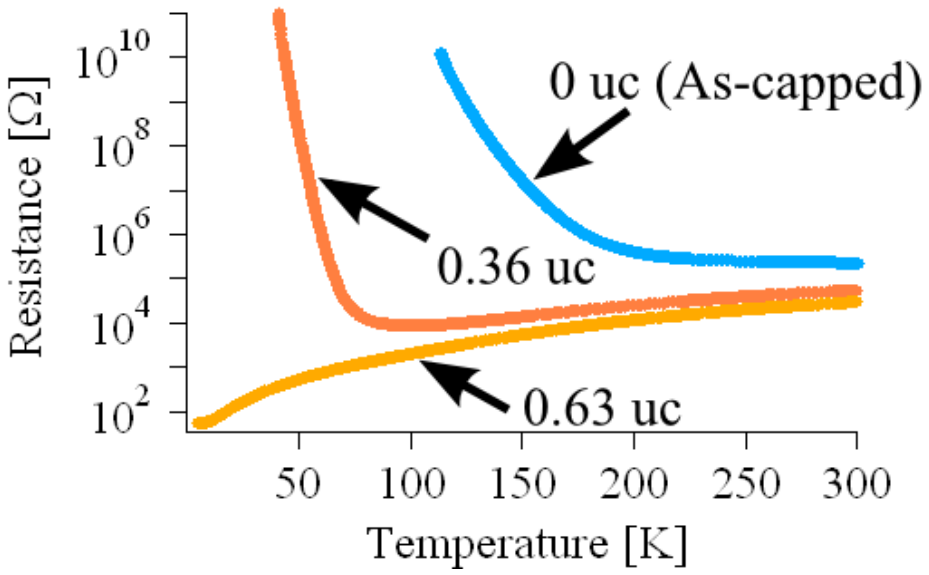

Figure 5.2: Temperature dependence of resistance for different $LaTiO_3$ coverages: 0.36 uc, 0.63 uc and 0 uc (as-capped) deposited at 900°C.

Fig. 5.2 shows the temperature dependence of resistance for different nanodot densities, given in terms of average coverage. The resistance measurements were done along the surface step normal direction. This is important to note for the 900°C samples, because there is also a small element of step-flow growth, which may result in nanowires forming along the surface step edges. Resistance measurements parallel to the step direction may thus be affected by the presence of metallic nanowires that make long-range connections through the sample. Transport

measurements were therefore done perpendicular to the step edges, because in this geometry, the influence of the nanowires is less significant. Further discussion on this point is in Sec. 4.2.

The $LaTiO_3$ nanodot coverage estimated from RHEED was 0.36 uc and 0.63 uc. An additional reference sample was made with a $SrTiO_3$ capping layer but without depositing the $LaTiO_3$ layer. Insulator (0.36 uc) and metallic phases (0.63 uc) can be seen in Fig. 5.2. The difference between the 0 uc and 0.36 uc shows that the resistance change is caused by the $LaTiO_3$ dots.

Repeatability

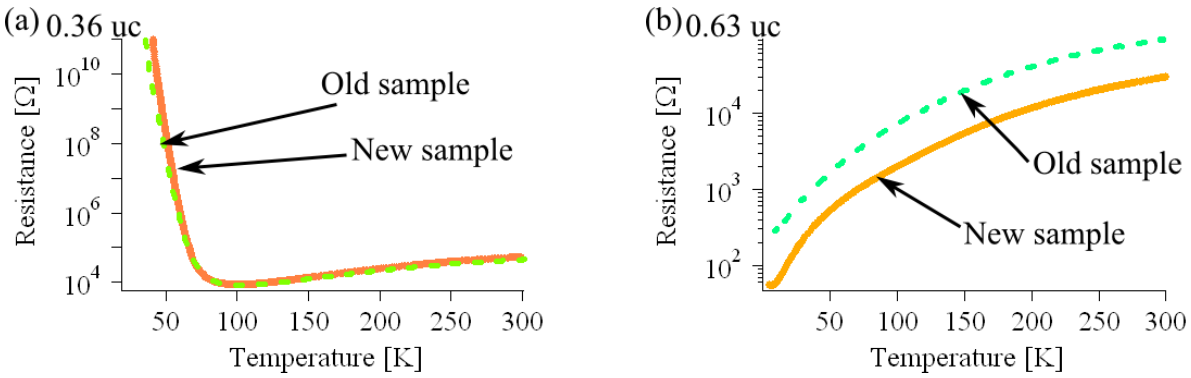

Figure 5.3: Comparison of two $LaTiO_3$ nanodot array samples grown at 900°C in two separate deposition runs with a three-month interval. The coverage is (a) 0.36 uc and (b) 0.63 uc.

The nanodot array contain only a single fractional layer of $LaTiO_3$ at an interface covered with a thin $SrTiO_3$ capping layer. As the purpose of the experiments is to study the critical behavior at a boundary between the insulating and metallic phases, the nanodot coverage has to be accurately controlled. However, the actual nanodot morphology cannot be verified in the transport samples. One way to increase confidence in the estimated coverage values is to check the repeatability of experiments. Fig.5.3 shows comparisons of resistance measurements done on samples similar to those illustrated in Fig. 5.2. Two samples with the same target coverage were fabricated in two deposition runs three month apart. The samples obtain in separate experiments showed that the deposition parameters could be accurately reproduced and there was no major difference in the observed temperature dependence of resistivity. The difference between the old and new 0.63 uc samples (Fig. 5.3(b)) is a constant shift on the log scale, which indicates that the resistance differ by a multiplicative factor that is not dependent on temperature. This is likely to be caused by a small difference in the electrode geometry, rather than an actual resistance behavior of the nanodot array. Especially for wire-bonded contacts, it is

difficult to control accurately the electrode distance and the contact area. It is thus reasonable to conclude that the deposition process repeatability is good and it unlikely that random coverage errors would significantly affect the conclusions of the work.

Direction dependence

As was mentioned earlier, high-temperature growth may also lead to the formation of nanowires on the surface. It is thus reasonable to ask what the effect of long metallic wires would be on the transport data obtained from such samples. This question can be answered by measuring the temperature dependence of resistance in various in-plane directions, as shown in Fig.5.4. The in-plane direction labeling follows Fig. 4.15 in Sec.4.2. The samples re the same as in Fig. 5.2. The metallic and insulator phases are observed regardless of the measurement direction, indicating that the nanowire formation is not complete and thus has little effect on the transport measurements.

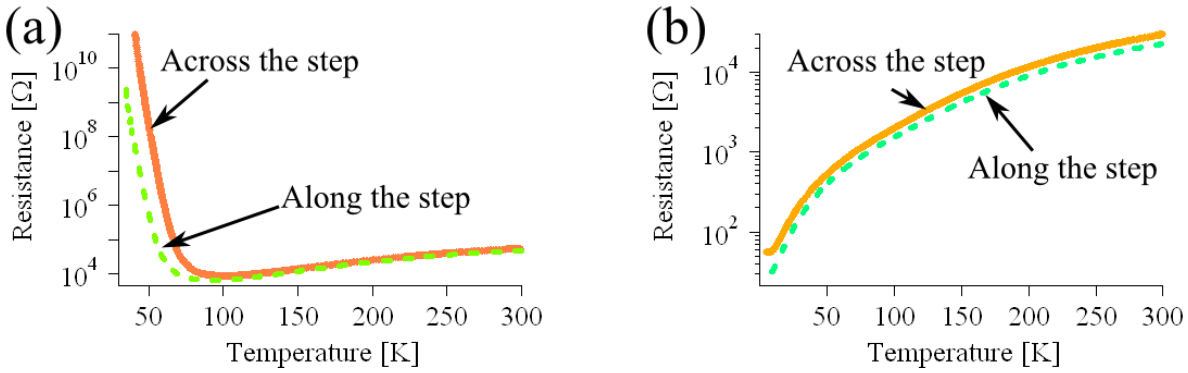

Figure 5.4: In-plane direction dependence of sample resistance for $LaTiO_3$ deposition at 900°C. Current flow is either parallel or perpendicular to the surface steps, as defined in Fig. 4.15. The nanodot coverage is (a) 0.36 uc and (b) 0.63 uc.

5.2.2 Topography property

AFM analysis

Fig. 5.5 shows AFM images of two samples where the $LaTiO_3$ nanodots were deposited at 900°C. These samples are the morphology analysis counterparts of the transport measurement samples in Fig. 5.2. The $LaTiO_3$ deposition conditions were thus the same as for the samples in Fig. 5.2. The nanodot coverage is (a) 0.36 uc and (b) 0.63 uc, as estimated by RHEED. Image sizes are 1000×1000 nm^2. The AFM images show that at 900°C, some of the $LaTiO_3$ nanodots

are attached to the step edge the top side of the step edges show a region that has no dots. This is the effect of developing step flow, where migrating surface atoms preferentially attach to the step edges.

A clear dot size difference between Figs. 5.5(a) and 5.5(b) was also observed, although the growth temperature was the same. The main parameter that affects the average dot size at a given temperature is time. The dot sizes can thus vary to some extent due to different amount of times that a sample is kept at the growth temperature. Even if the processing times, such as heating and cooling delays and rates are kept equal, the total growth time is different, since the coverage changes are achieved by changing the ablation laser pulse count. The laser pulse rate was fixed at 2 Hz and doubling the coverage thus also doubles the deposition time, which results in an increase of the average dot size. The $LaTiO_3$ dots can thus grow while the deposition is proceeding, because the substrate stays at high temperature. In the case of the samples shown in Fig. 5.5, the deposition time difference between the two samples was 6.5 seconds.

Another aspect that affects the dot growth is the reduction of the average diffusion length for surfaces with higher coverage, as the average dot distance becomes smaller. For freshly-deposited adatoms it thus becomes easier to find stable attachment sites at nearby dot edges, rather than nucleate a new nanodot. This problem is described and confirmed by experiment in Sec. 5.4.

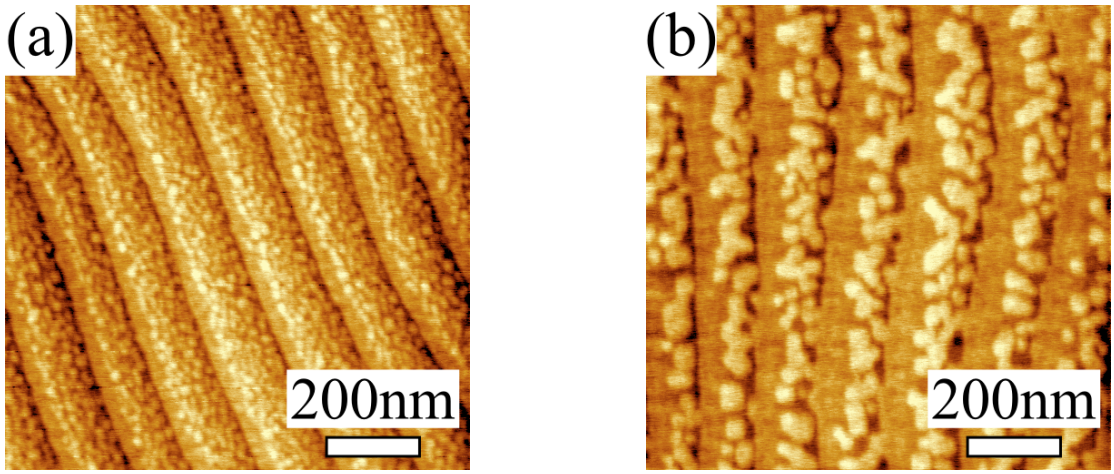

Figure 5.5: AFM images of $LaTiO_3$ dot arrays deposited at 900°C. The image size is 1000 × 1000 nm^2. The coverage is (a) 0.36 uc and (b) 0.63 uc, estimated by RHEED.

STM analysis

Fig.5.6 shows STM images of samples where $LaTiO_3$ nanodots were deposited at 900°C. The samples are the same as those used for the AFM analysis, shown in Fig. 5.5. The corresponding

transport data is in Fig. 5.2. The image sizes are 250×250 nm^2. The coverage is (a) 0.36 uc and (b) 0.63 uc. For these samples, the coverage could not be estimated accurately from the STM images (Fig.5.6) because some of the deposited $LaTiO_3$ was attached to the $SrTiO_3$ substrate steps and it was not possible to determine from the topography images the edge of the original $SrTiO_3$ terrace edge. However, the main advantage of the STM is that smaller dots can be imaged and even for the larger dots, the spacing between dots can be accurately imaged. A third advantage of the STM is that it is possible to detect the morphology within individual dots. While AFM shows the size and shape of the dots, it is difficult to measure the height. Height profiles along the gray lines in Fig. 5.6 are shown in Fig. 5.7. The $LaTiO_3$ island height can be measured as 1 uc because of the following reason. Both $LaTiO_3$ and $SrTiO_3$ have nearly the same lattice parameter (Sec.3.3). It is the possible to compare the island height with the $SrTiO_3$ step edge height, which is known to be a single unit cell. Fig. 5.7 shows that the island height is equal to the step height, and is thus 0.4 nm.

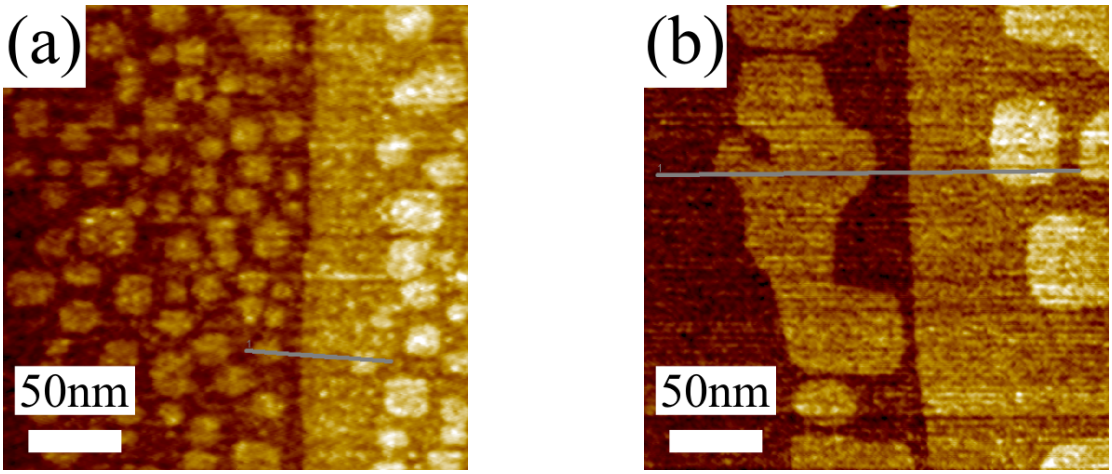

Figure 5.6: STM images of $LaTiO_3$ nanodot samples deposited at 900°C. The image size is 250×250 nm^2. Coverage is (a) 0.36 uc and (b) 0.63 uc. The STM imaging conditions were (a) $V = 5.50$ V $I = 990$ pA, (b) $V = 4.50$ V $I = 900$ pA.

5.2.3 Discussion

$LaTiO_3$ nanodot arrays grown at 900 °C showed a clear electronic phase change in transport (Fig. 5.2) and the metal-to-insulator change could be correlated with a difference in the surface coverage by $LaTiO_3$ nanodots (Figs. 5.5 and 5.6). For the purpose of measuring electron spread in the $SrTiO_3$ substrate under the $LaTiO_3$ dots, samples deposited at 900°C are problematic for several reasons.

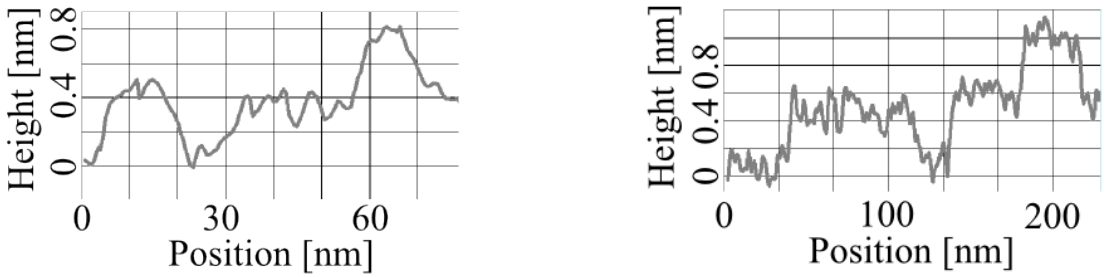

Figure 5.7: Surface height profiles taken along the dark lines in Fig.5.6.

Most importantly, large $LaTiO_3$ dots results in agglomeration of islands, which means that the variation in island sizes becomes large. It is thus no longer to assign an average island size to a surface. This problem can be seen in Fig. 5.6, which shows only a small number of individual $LaTiO_3$ nanodots, making statistical analysis difficult. Another issue caused by very large islands is related to the attachment of islands to step edges, finally developing long wire structures along the surface steps. This type of surface morphology creates two difficulties for transport measurement. Measurements along the step edge direction would become less sensitive to percolative transport between dots and is dominated by conduction along the step edges. In a perpendicular direction, the nanowire formation also causes a region on the terraces that does not contain any dots. There is thus a periodic break in the nanodot array, and the breaks become progressively wider as the nanowire formation becomes dominating. The nanowire formation also creates difficulties for accurate coverage determination from the STM images.

The conclusion thus is that a slightly lower growth temperature may be more appropriate for determining the critical coverage for a metallic nanodot array.

5.3 800°C $LaTiO_3$ deposition

As explained in Sec. 5.2.3, nanodot growth at 900°C resulted in samples that showed clear transport transition, but the structural characterization was complicated by a nonideal nanodot morphology distribution. Similar experiments were therefore performed for arrays with smaller average dot sizes, grown at 800°C.

5.3.1 Transport property

Coverage dependence

the coverage dependence for nanodot arrays grown at 800°C were measured. As shown in Fig.5.8, the transition to metallic state occurred at a lower coverage than for the 900°C samples. The nanodot coverages of 0.13 uc, 0.38 uc, and 0.62 uc were estimated from the RHEED data. The insulating phase was seen for the 0.13 uc sample, while both the 0.38 uc and 0.62 uc sample showed a very similar metallic temperature dependence of resistance. The difference in the critical coverage is probably caused by the difference in the nanodot morphology.

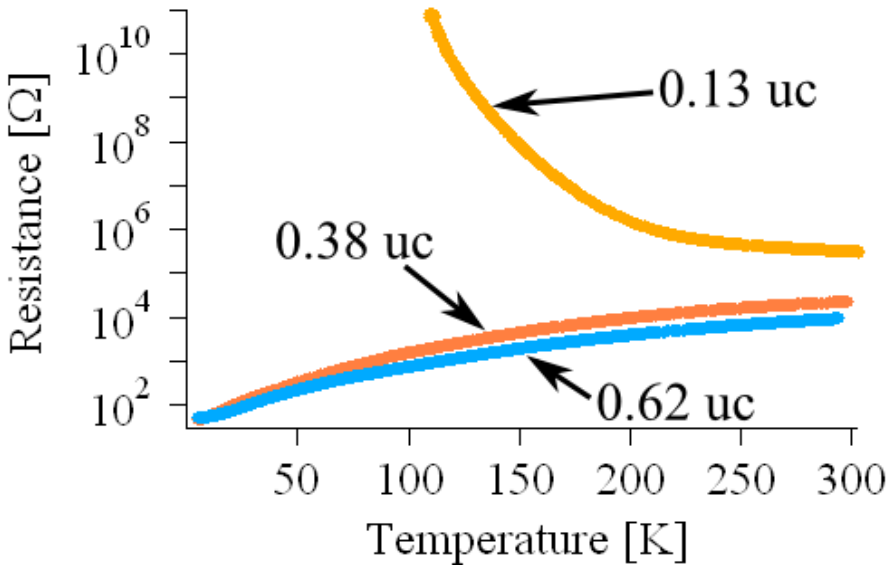

Figure 5.8: Coverage dependence of transport for a $LaTiO_3$ nanodot array grown at 800°C. The nanodot coverage was 0.13 uc (Insulator), 0.38 uc (metallic) or 0.62 uc (metallic). The coverage was estimated by RHEED.

Direction dependence

A small but systematic difference was seen in the resistance of nanodot arrays grown at 900°C when the current path was either perpendicular or parallel to the step edges. Fig. 5.9 shows the results of a similar measurement for two nanodot arrays grown at 800°C. The current flow direction is defined in Fig. 4.15). The nanodot coverage was (a) 0.13 uc and (b) 0.38 uc. Comparison with samples deposited at 900°C (Fig. 5.4), the direction dependence is clearly smaller for the nandot array grown at 800°C. It thus appears that the step-flow component that caused the appearance of nanowires, is no longer affecting transport in the lower-temperature growth. The presence of metallic nanowires is expected affect the insulating samples more than the metallic samples and may, in part, cause the shift to lower critical coverage for the 800°C arrays.

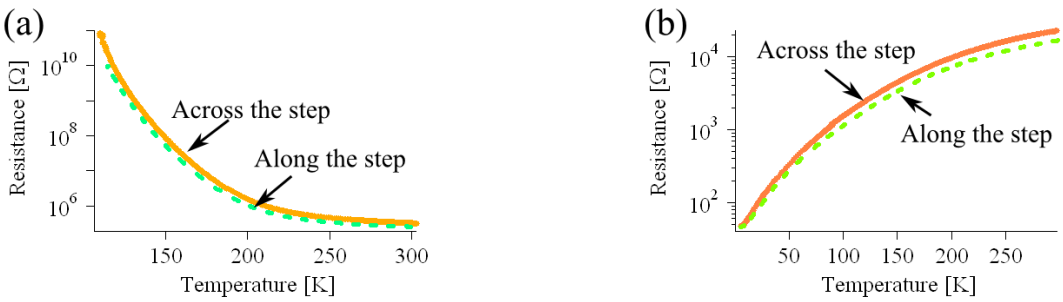

Figure 5.9: Direction dependence of resistance in for $LaTiO_3$ nanodot arrays deposited at 800°C. Current direction labels follow Fig. 4.15. The nanodot coverage is (a) 0.13 uc and (b) 0.38 uc.

5.3.2 Topography

AFM images

AFM images of two dot arrays grown at 800°C are shown in Fig. 5.10. The coverage was (a) 0.13 uc (insulating) and (b) 0.38 uc (metallic). The image size is 1000×1000 nm^2. Although the presence of nanodots is clearly observable in both cases, coverage analysis cannot be accurately performed based on the AFM images because the finite size of the AFM tip results in an increased apparent dot size in the images. The AFM images were mostly used to quickly verify that a dot array was actually obtained. The images also sow that there is no difference in island density in the middle of a trace and close to the step edges. It is thus safe to conclude that there is no contribution from nanowires. The surface morphology is thus consistent with the lack of directional resistance differences in these samples.

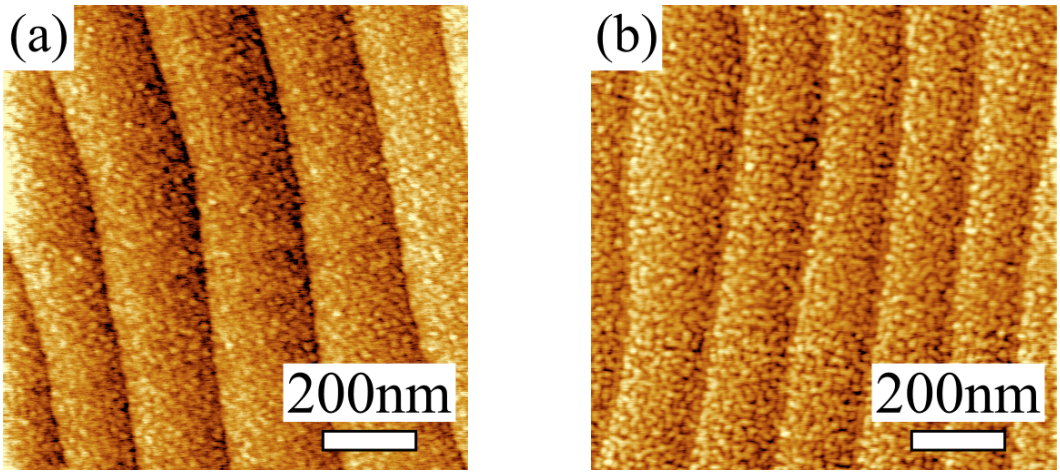

Figure 5.10: AFM image of $LaTiO_3$ nanodot arrays deposited at 800°C. The coverage is (a) 0.13 uc and (b) 0.38 uc. Image size is 1000×1000 nm^2.

STM image

While the difference in the nanodot structure was hard to see in the AFM images, the dot sizes and shapes are much more easily visible in the corresponding STM images, shown in Fig.5.11. The nanodot samples are the same as those shown in fig.5.10. The coverage is (a) 0.13 uc and (b) 0.38 uc. The STM imaging conditions were (a) $V = 3$ V, $I = 30$ pA and (b) $V = 3$ V, $I = 30$ pA. It is clear that the $LaTiO_3$ dot distribution is more equal than at 900°C (Fig. 5.6). Variations in dot size are also smaller, particularly at low coverage. The height profiles in Fig. 5.12 show that the dot height is still 1 unit cell, the same as the substrate step height. These samples are thus better suited for the analysis of electron spread around the nanodots.

5.3.3 Coverage analysis

The smaller and more regular dot morphology, and the lack of nanowire formation, made it possible to calibrate the surface coverage estimated from RHEED oscillation data against surface STM images. The coverage was estimated from 3 separate images for each coverage to obtain better statistics. This is necessary due to the limited scan range of the STM. One of the images used for dot area analysis is shown in Fig. 5.13. The image size is 100×100 nm^2. The images were automatically segmented and labeled by SPM image processing software. The coverage estimated from the STM images was 20% for the 0.13 uc sample and 46% for the 0.38 uc sample. The difference is small and is mostly caused by the difficulty of measuring accurate coverage by RHEED oscillation monitoring. The main source of error is caused by the fact the RHEED oscillation maximum does not correspond to a layer thickness of exactly 1

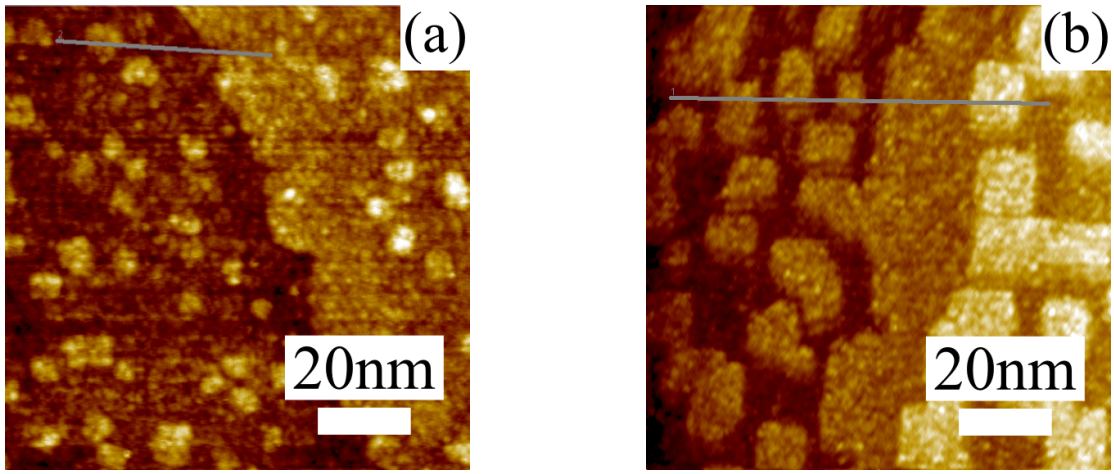

Figure 5.11: STM images of $LaTiO_3$ nanodot arrays grown at 800°C. The coverage is (a) 0.13 uc and (b) 0.38 uc. The STM imaging conditions were (a) $V = 3$ V, $I = 30$ pA and (b) $V = 3$ V, $I = 30$ pA. Image size is 100×100 nm^2.

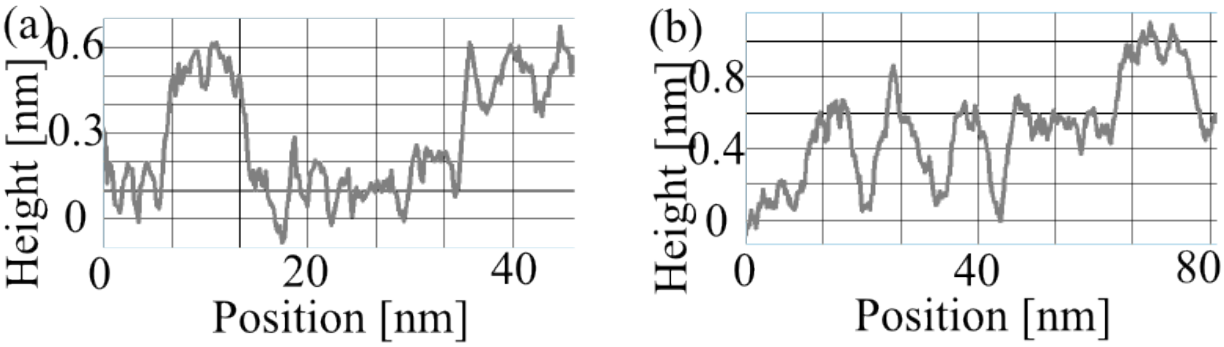

Figure 5.12: $LaTiO_3$ dot height profiles, taken along the dark marker lines in Fig. 5.11.

unit cell. The average $LaTiO_3$ dot are was 17.9 nm^2 for the 0.13 uc sample and 381 nm^2 for the 0.38 uc sample. The dot size difference is caused by the same mechanisms that were discussed in Sec. 5.2.2.

The STM images were also used to analyze the distance between neighboring nanodots. From the point of view of transport behavior change, the average distance of nanodots is more important than the average coverage. The $LaTiO_3$ dot distance distribution histograms were therefore constructed as shown in Fig. 5.14. The data for the histograms was collected from 8 STM images each for both the 0.13 uc and 0.38 uc samples. This allowed enough dot distances to be measured for constructing a histogram with a sufficiently small bin size. The number of data points was 721 in (a) and 332 in 332 in (b). The Y axis is normalized. The $LaTiO_3$ nanodots do not have a minimum finite distance, but the noise in the STM data prevents accurate distance

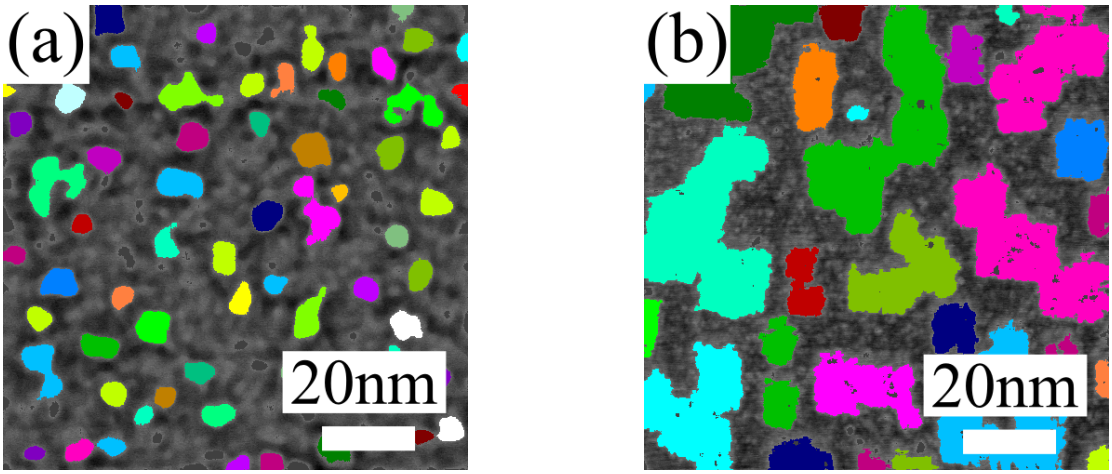

Figure 5.13: Coverage estimation from STM images. The image size is 100×100 nm^2. The estimated coverage was (a) 20% (0.13 uc) and (b) 46% (0.38 uc).

measurement for dot distances of less than about 1 nm. It is occasionally difficult to determine from the image if two nanodots are connected or a small atomic-scale gap still exists. The data in the histograms is therefore unreliable for length scales of less than 1 nm. What the histograms in Fig. 5.14 do show is that the dominant $LaTiO_3$ dot distance in (b) is clearly narrower than in (a). This means that the average distance between nanodots is smaller for higher coverage. It thus appears that the metallic phase in the 0.38 uc dot array (Fig. 5.8(b)) is caused due to the dominance of $LaTiO_3$ dot distances below about 2 nm. Half of that value would be about 1 nm. It is thus possible to conclude that the order of magnitude for the electron spread in $SrTiO_3$ under the $LaTiO_3$ dots is 1 nm. This is the same order of length of Ti valence variation observation at $SrTiO_3$/ $LaTiO_3$/$SrTiO_3$ [44].

5.3.4 Discussion of dot size

In percolation theory, the model behavior is determined by the value of the probability, p, of a model element in being in one of two states, such as a metal or an insulator. In the analysis of percolation in the $LaTiO_3$ nanodot array, p is a function of the conductive surface area, which is larger than the physical nanodot area due to the lateral spread of carriers beyond the physical confines of a single nanodot. This is important for considering dot size. Fig.5.16 shows the difference in the total conductive area for different $LaTiO_3$ dot sizes for the same nominal nanodot coverage. It is clear that the total $SrTiO_3$ conductive area is different for the two cases.

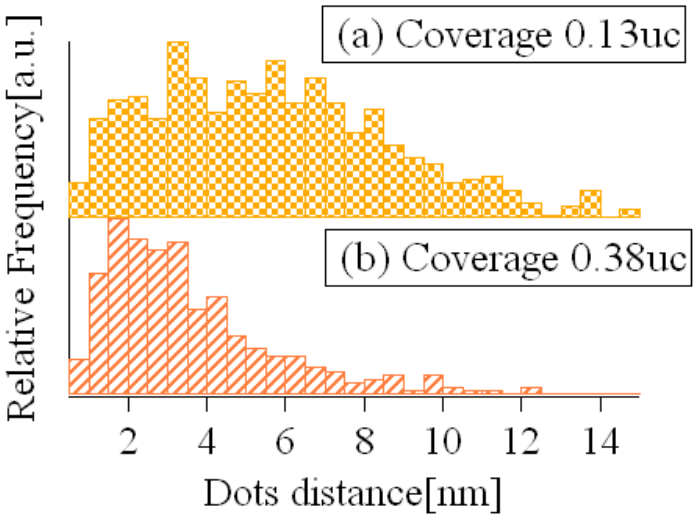

Figure 5.14: Histograms of $LaTiO_3$ dot distances obtained from $LaTiO_3$ nanodot arrays grown at 800°C. The $LaTiO_3$ coverage is (a) 0.13 uc and (b)0.38 uc.

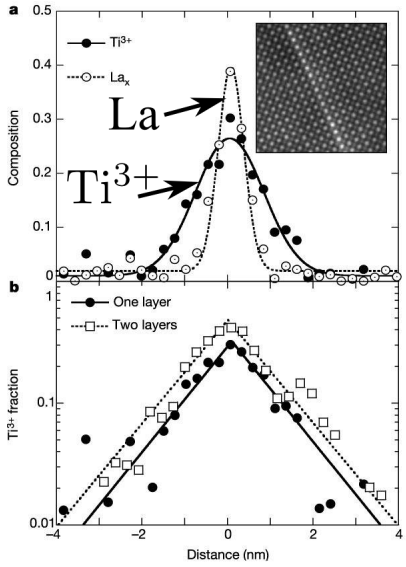

Figure 5.15: Ti^{3+} distribution around $SrTiO_3/LaTiO_3/SrTiO_3$ structure[44]

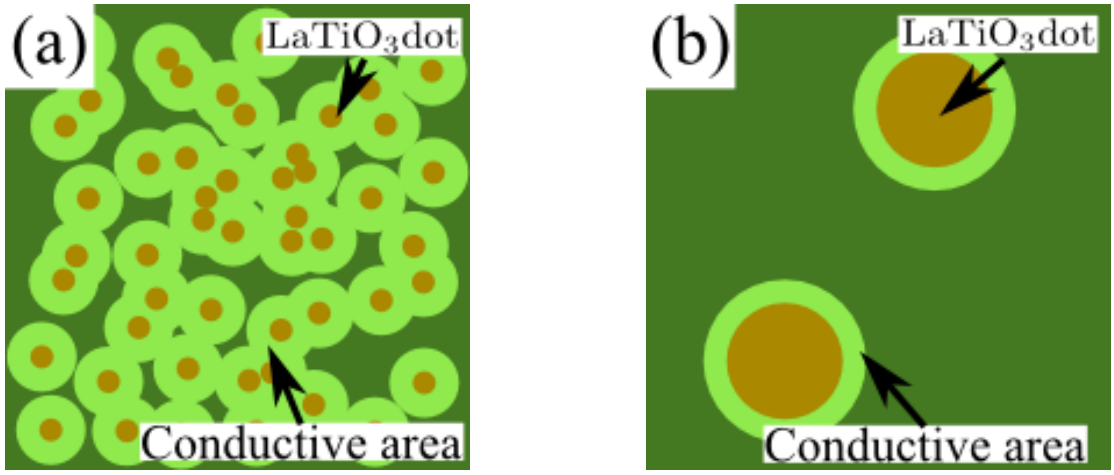

Figure 5.16: Comparison of the total conductive area for two different dot sizes for constant coverage.

$SrTiO_3$ conductive area calculation

This conductive area can be estimated with a simple calculation. If the parameters are set as $LaTiO_3$ radius: r_{LTO}, electron spread distance:l_e, $LaTiO_3$ dot coverage:n_{LTO}, conductive area coverage:$n_{conduct}$, number of $LaTiO_3$ dots:c_{LTO}, and the size of the whole area:S. The following

relations hold:

$$n_{LTO} = \frac{c_{LTO}\pi r_{LTO}^2}{S}, \tag{5.1}$$

$$n_{conduct} = \frac{c_{LTO}\pi (l_e + r_{LTO})^2}{S}. \tag{5.2}$$

From these equations, the following relation can be obtained,

$$n_{conduct} = n_{LTO}\left(1 + \frac{l_e}{r_{LTO}}\right)^2. \tag{5.3}$$

In this equation, the overlap of the $SrTiO_3$ conductive area surrounding different $LaTiO_3$ dots is ignored and the $LaTiO_3$ dots are assumed to be circular. It can be seen from Eq.5.3 that the $SrTiO_3$ conductive area coverage depends not only on the $LaTiO_3$ dot area density but also on the electron spread distance and the $LaTiO_3$ dot size. Because the conductive area overlap is ignored, Eq.5.3 can not be used for high $LaTiO_3$ nanodot densities.

Effect of conductive area $LaTiO_3$ dot size dependence to percolation theory

Analysis of percolative conductivity only depends on the total conductive area. Fig.5.17 shows an example of a 2-dimensional percolation model for conductivity analysis. The black and white boxes denote metallic and insulating particles. Conductivity of the system depends on the ratio of black and white boxes, usually expressed as the probability p of an arbitrary box being metallic (black). When applying this model to the nanodot array analysis, the black boxes represent the conductive area. Because conductive area size depends on the $LaTiO_3$ dot size in addition to dot coverage, conductivity cannot be accurately analyzed by percolation theory that is parametrized by dot size when nanodot arrays with different average dot sizes are compared. The conductive area coverage is a linear function of nanodot coverage around the critical percolation limit only if the $LaTiO_3$ dot size is independent of nanodot coverage, as explained Eq.5.3.

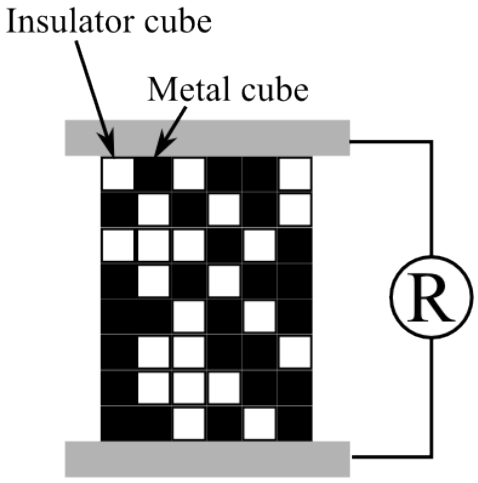

Figure 5.17: 2-dimensional percolative conductivity model for a mixture of metallic (black) and insulating (white) particles.

5.4 Dot size control

5.4.1 Dot size change observation

The nanodot arrays discussed in the previous section showed that a clear transition does occur from an insulating to a metallic state as the nanodot coverage is increased. A critical dot distance estimate could also be obtained. However, while the samples discussed so far have different nanodot coverages, the samples also have different nanodot sizes (Fig. 5.13).

It is therefore not clear what the influence of dot size change is on transport for a given $LaTiO_3$ coverage. A naive application of percolation analysis would imply that the nanodot size should not have a significant effect on the critical coverage. Experiments, however do show a large critical coverage difference for the 800°C and 900°C nanodot arrays with dramatically different island sizes. It is thus still an open question what would be the correct statistical parameter for parameterizing a percolation model (Sec. 1.4.2). [59].

As explained in Sec. 5.2.2, the nanodot size depends on the total $LaTiO_3$ deposition time, in addition to coverage. Samples with larger coverage take longer to grow, increasing the average dot size. It should thus be possible to control the dot size independently of coverage if the surface migration process is separated from the deposition process. Fig. 5.18(a) shows the temperature profile of a sample during the nanodot array fabrication at a fixed temperature. The length of the deposition phase varies from sample to sample, depending on how large the desired total deposited $LaTiO_3$ amount is.

A different process was therefore adopted, where the deposition is performed at a much lower temperature, followed by a suitable high-temperature anneal. As shown in Fig. 5.18(b), the deposition of $LaTiO_3$ was done at a fixed temperature of 500°C. At this temperature, there is almost no dot growth over time, as shown by the initial AFM study. The growth anneal process can be accurately controlled, either by changing the annealing temperature or time. The deposition time variation problem can thus be resolved by this process.

In the growth anneal process, the main dot size control parameter is the annealing time. Although both temperature and time can change the surface migration rate, it is technically more simple to fix the temperature so that the necessary annealing times are in the range of minutes. Dot size control was attempted for two coverages, 0.15 uc and 0.39 uc. Results of experiments where nanodot arrays were annealed at 800°C for 1 min, 10 min or 30 min are shown in Fig. 5.19. It is clear that the dot size increased systematically with the annealing time, while the dot density reduced. The reduction of nanodot density and an increase of average dot distance is especially clear for the 0.15 uc sample. The surface migration is quite fast at 800°C. As shown by the AFM image in Fig. 5.19(d), clear dots can be seen after an annealing time of

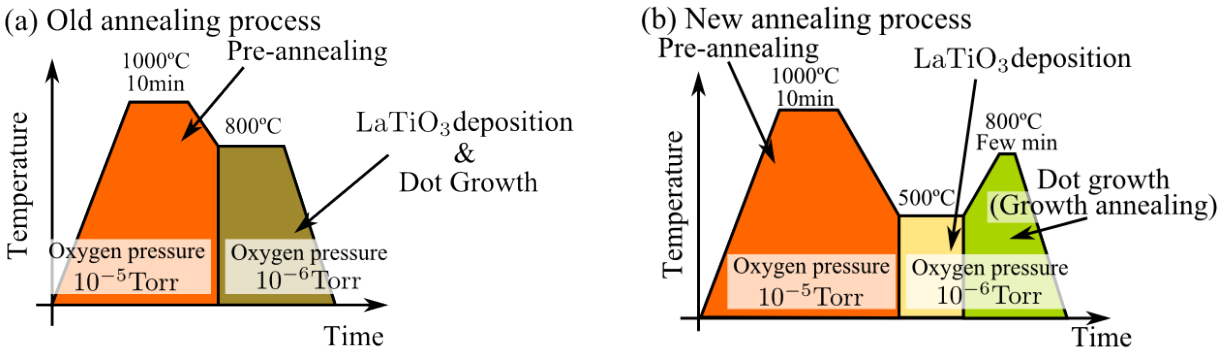

Figure 5.18: (a) A process time-temperature diagram for a simple deposition process. The deposition time is proportional to the desired coverage. (b) A deposition-anneal process, where the deposition and anneal procedures are separated.

just 1 minute. For the 0.15 uc sample (Fig. 5.19(a)), a 1-minute annealing time did not produce large enough dots to be observed by AFM. However, the dot structure is easily visible in STM images, as shown in Fig. 5.20. The height profile shows that for the small dots there is still significant probability for double-layer structures to form. This happens for low-temperature deposition, where the surface migration rate is very low. Single unit cell islands therefore form only during higher-temperature annealing.

The AFM data in Fig. 5.19 can be used to select suitable annealing conditions to obtain comparable dot arrays. For example, by picking samples illustrated in Figs. 5.19(c) and 5.19(d), it is possible to compare samples with nearly the same dot size but different coverage.

The nanodot growth process occurs through surface migration and is thus dependent on the average migration path length between adjacent nanodots. For lower coverage, the average dot distance is larger, leading to a slower ripening process.

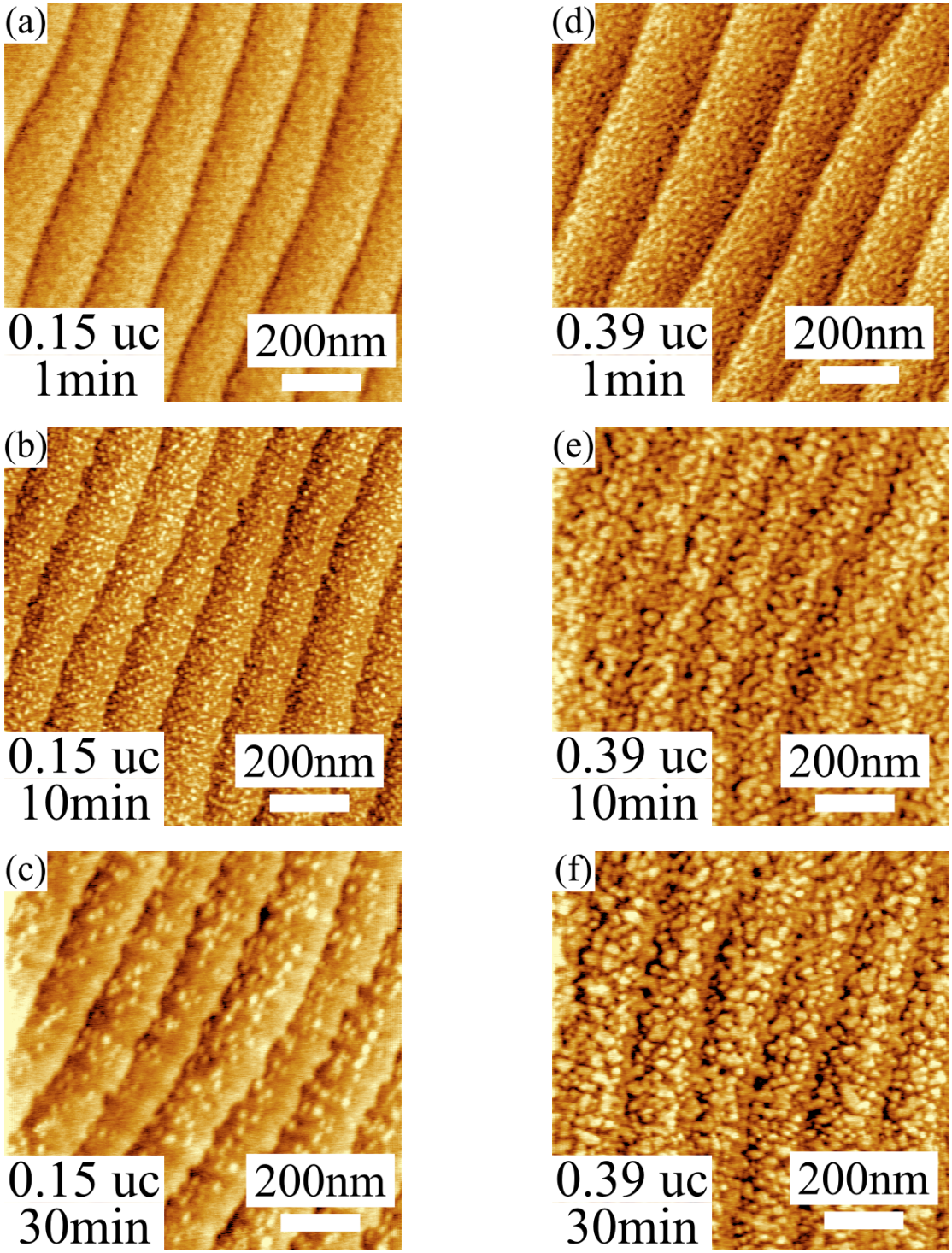

Figure 5.19: The effect of annealing at 800°C on the size of $LaTiO_3$ nanodots grown at 500°C. The annealing time is (a)(d) 1 min, (b)(e) 10 min, and (c)(f) 30 min. The coverage is (a)(b)(c) 0.15 uc and (d)(e)(f) 0.39 uc.

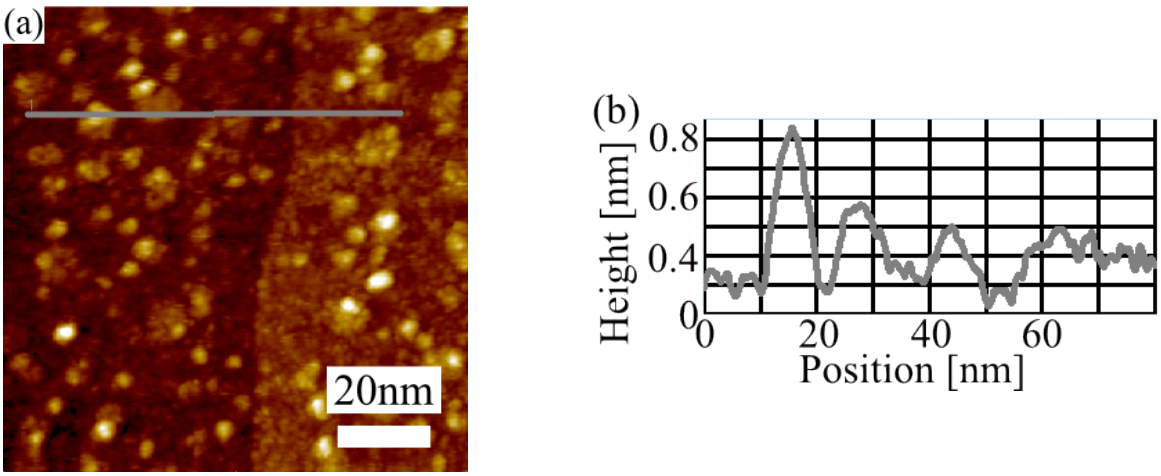

Figure 5.20: (a) STM image of 0.15 uc coverage $LaTiO_3$ nanodot sample grown at 500°C and annealed at 800°C for 1 min. This is the same sample as in Fig. 5.19(a). (b) Height profile along the solid line in (a).

5.4.2 Dot size relation

For nanodot size control, a suitable annealing time needed to be determined independently for each desired coverage, since the dot size is a function of both anneal time and total $LaTiO_3$ coverage,

$$S = S(t, \theta), \tag{5.4}$$

which should be constant in this experiment. As the purpose was to obtain a series of samples with different nanodot coverages but a constant average dot size, it was necessary to determine the relationship between annealing time and average coverage for a given dot size,

$$t = t(\theta). \tag{5.5}$$

To determine $t(\theta)$, the process that controls the dot size needs to be analyzed. The dot size is determined by the opportunity of adatoms encountering each other during surface migration. This process can be explained by lateral flow. the number of adatoms that flow into a circle surrounding an arbitrary adatom is illustrated in Fig.5.21. If the materials are the same, the opportunity for an encounter between adatoms is determined by the total number of adatoms flowing into the region surrounding another adatom. The relation between time and coverage, $t(\theta)$, can be obtained by considering the number of such adatoms.

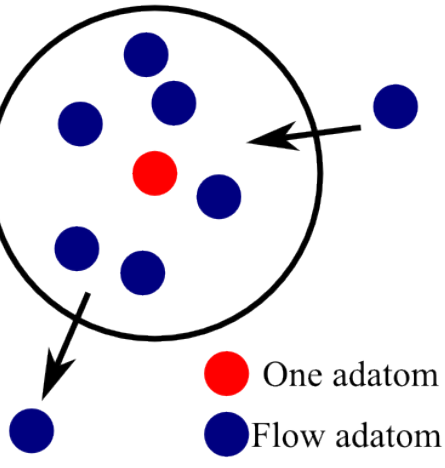

Figure 5.21: Illustration of migrating adatoms moving into or out of a circle surrounding an arbitrary adatom.

The annealing time and the effect of coverage on the adatom flow is considered. The annealing time is affected by the average migration length. Because the migration length is determined by a random walk process, the time dependence of migration distance is given by

$$L \propto \sqrt{t}. \tag{5.6}$$

The total adatom coverage affects the number of adatom flow. If a circle around a specific adatom has a radius r, the number of adatoms in circle is given by

$$N = \pi r^2 \theta, \tag{5.7}$$

where θ is the coverage and is equal to the density of adatoms on the surface. The following relations can be derived from this equation:

$$r_N = \sqrt{\frac{N}{\theta\pi}}, \tag{5.8}$$

$$r_N \propto \frac{1}{\sqrt{\theta}}, \tag{5.9}$$

where r_N is the radius that contains N adatoms. To maintain a constant number of adatoms in the vicinity of a given nanodot, the migration length and radius need to be of the same order,

$$\frac{L}{r_N} \propto \frac{\sqrt{t}}{\frac{1}{\sqrt{\theta}}} = \sqrt{t\theta} = c\text{:constant}, \tag{5.10}$$

$$t = \frac{c^2}{\theta} \tag{5.11}$$

which means that the annealing time decreases rapidly with coverage.

5.4.3 Dot size control

To obtain an expression for the annealing time dependence, a simple model will be sufficient, with time calculated as $t = \exp(a\theta + b)$.

Fig.5.22 shows AFM images of a set of samples with different coverages. The coverages and annealing times are: (a) 0.14uc 673s, (b) 0.20uc 414s, (c) 0.25uc 260s, (d) 0.30 uc 167s, and (e) 0.36uc 112s. The dot size is still small, even in the high coverage samples. The dot size radius is estimated from the topography images and Fourier transforms of the images. A Fourier transform is needed to analyze the high coverage samples because small dots tend to stick to each other as show Fig.5.22 (f). This small dots cannot be distinguished as individual dots by conventional particle detection algorithms. However, a Fourier transform is still useful

for determining the dot size because high coverage because the dot attachment has a small effect on the characteristic spatial frequencies in the images.

Fig.5.23 shows images obtained by Fourier filtering of the original AFM topography data. The Fourier filter limits were set so that the inverse Fourier images reproduced the nanodot structure of the original image. The Fourier filter bounds were used as the average dot size estimate for 0.25uc, 0.30uc, 0.36uc sample. the dot diameters d were calculated for each coverage as 0.14 uc: 14 ± 4nm, 0.20uc: 15 ± 7nm , 0.25uc: $7 < d < 25$nm, 0.30 uc: $6 < d < 17$nm, 0.36uc: $6 < d < 32$ nm. Because the dot sizes are all of the same order, it can be concluded that the dot size control was successful.

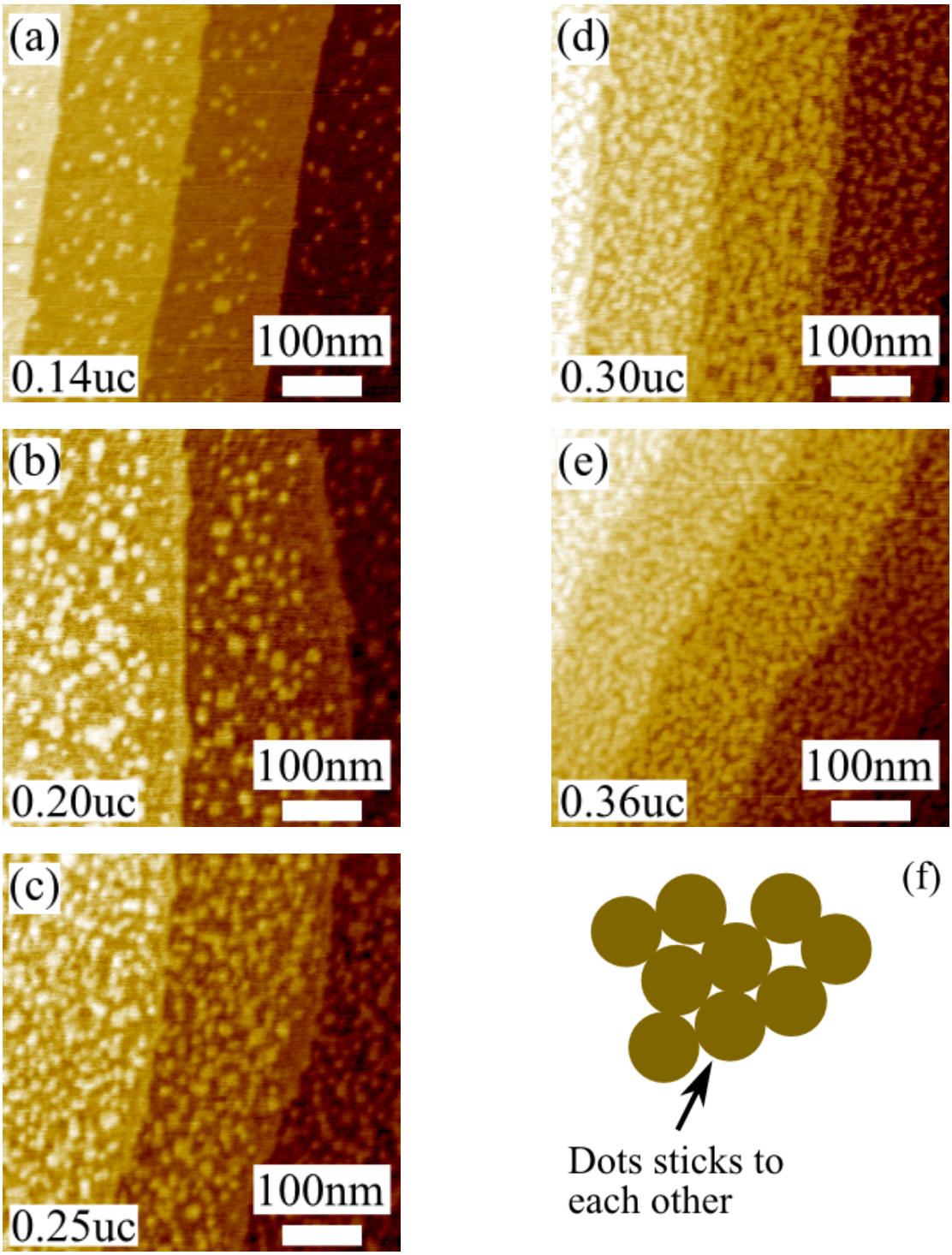

Figure 5.22: The effect of annealing nanodots at 800°C on the size of $LaTiO_3$ nanodots grown at 500°C and (f)image of nanodots. The coverage and annealing time is (a) 0.14uc 673s, (b) 0.20uc 414s, (c) 0.25uc 260s, (d) 0.30 uc 167s, and (e) 0.36uc 112s.

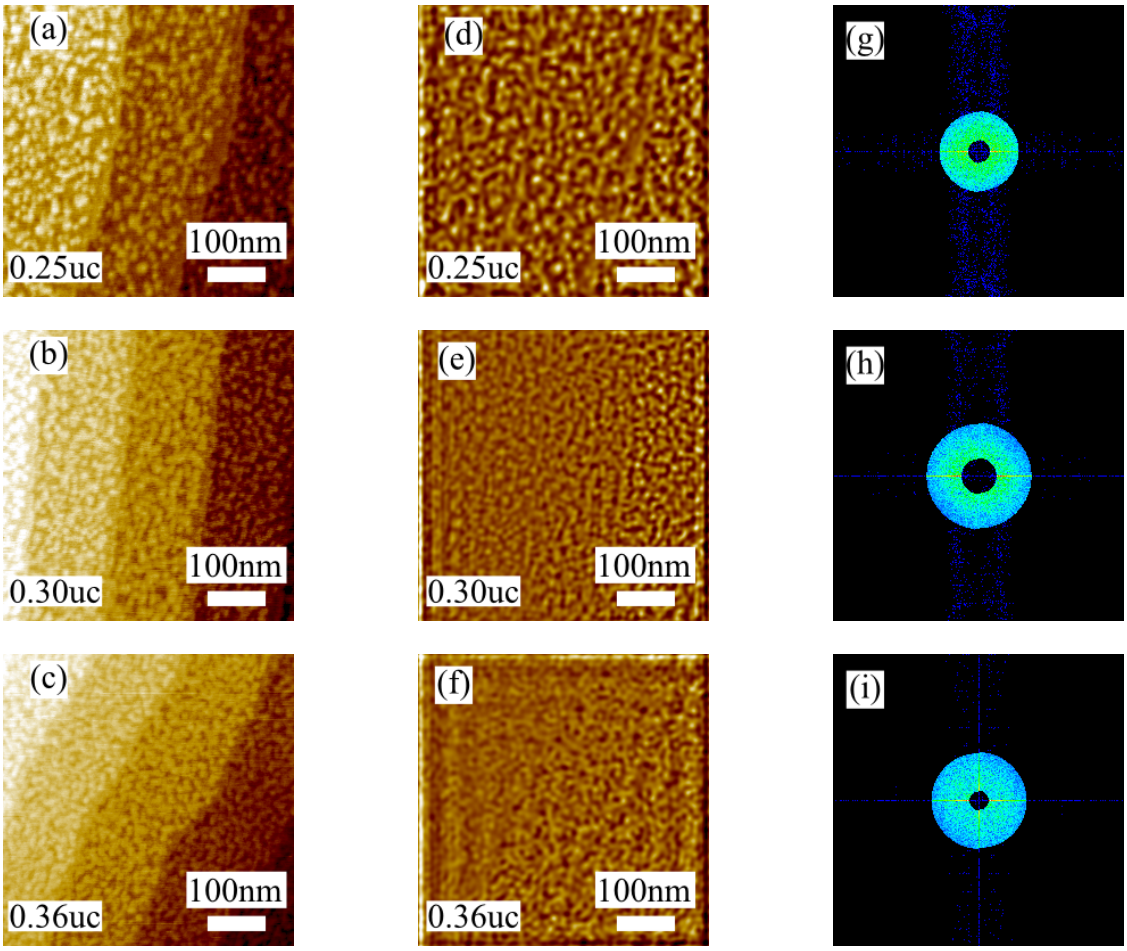

Figure 5.23: Raw image, inverse Fourier transform and Fourier transform images for (a)(d)(g) 0.25uc 260s, (b)(e)(h) 0.30 uc 167s, (c)(f)(i) 0.36uc 112s.

Chapter 6

Summary

Lateral electron spread around $LaTiO_3$ nanodots on a $SrTiO_3$ surface was estimated by comparing transport properties of nanodot arrays with the nanodot topography, specifically the average dot coverage. A change of $LaTiO_3$ dot size was observed for different $LaTiO_3$ deposition temperatures. The transport properties and surface topography were measured for 800°C and 900°C $LaTiO_3$ deposition temperatures. A transport behavior change from insulator to metal was observed between nanodot coverages of 0.36 uc and 0.63 uc for dot arrays grown at 900°C and between 0.13 uc and 0.38 uc for samples grown at 800°C. Repeatability of achieving the same coverage was checked by comparing nominally equivalent samples grown 1 month apart. Such repeatability checks were necessary to ensure that the *Transport sample* and *Topography sample* could be reliably compared. direction dependence was observed for *Transport sample*, indicating that $LaTiO_3$ wire structures were formed along the step edges at the 900°C growth temperature. The difference in the critical coverage between the 800°C and 900°C samples was found to be due to a difference in the average nanodot size. The $LaTiO_3$ dot height was equal to 1uc, as expected for lateral $LaTiO_3$ dot growth. Possible effects from 3-dimensional nanodot structures could thus be ignored. Coverages estimated from STM images and RHEED oscillations were 20% for 0.13 uc and 46% for 0.38 uc. This is a reasonable agreement, considering the limitations of RHEED intensity analysis for submonolayer coverage analysis. A dot distance histogram was calculated from the STM image data for samples grown at 800°C. The electron spread was estimated from the histograms as about 1 nm. This is the same order of magnitude as the Ti valence spread that has been reported previously.[44] A dot size difference was observed at different coverages. The $LaTiO_3$ deposition process and the $LaTiO_3$ nanodot lateral growth process were separated to prevent the $LaTiO_3$ growth time differences from affecting the average dot size for samples with different nanodot coverages. The dot size difference was found to invalidate simple conductivity analysis based on percolation theory as different dot

sizes lead to systematic differences in the ratio of the conducting surface area to the nanodot coverage. The growth and annealing process was applied to avoid the dot size differences for samples with different coverages.

Acknowledgments

At first, I would like to express my great gratitude to my advisor, Prof. Mikk lippmaa in the Department of Advanced Material Science, University of Tokyo for his continuing guidance, advice and encouragement in my master course. It would be impossible without his particular patience and courtesy to complete this thesis and research. I could not have imagined having a better advisor and mentor for my Master course study. Through daily discussion and his attitude to the research, I learned a lot of things, physics, experimental techniques and especially how interesting the science is. Dr. Ryota Takahashi, Dr. Mikko Matvejeff, Dr. Takayuki Harada, Dr. Kazunori Nishio were great supporting me in all experiment, especially for sample fabrication by Walkman chamber. Without their support, this thesis would not taken shape either. And I cannot express my gratitude by words to my collegue, Mr. H. Misumi, Mr. S. Kawasaki, Mr M. Ogawa Mr. T.Peltier and Mr. A.Yoshida for their kind supports and encouragement. I appreciate Ms. J. Kawamura for supporting office work.

Outsides the lab, I appreciate Prof. Hasegawa, Dr. T. Eguchi and Dr. Hamada for their cooperation to AFM, especially Tip etching and STP measurement.

Finally I would like to express my sincere gratitude to all of my friends and my family for the warm support and encouragement.

Bibliography

[1] T. An, T. Nishio, T. Eguchi, M. Ono, A. Nomura, K. Akiyama, and Y. Hasegawa. Atomically resolved imaging by low-temperature frequencymodulation atomic force microscopy using a quartz length-extension. *REVIEW OF SCIENTIFIC INSTRUMENTS*, Vol. 79, p. 03370, 2008.

[2] A. Bannani, C. A. Bobisch, and R. Möller. Local potentiometry using a multiprobe scanning tunneling microscope. *Review of Scientific Instruments*, Vol. 79, p. 083704, 2008.

[3] M. Basletic, J.-L. Maurice, C. Carrétéro, G. Herranz, O. Copie, M. Bibes, É. Jacquet, K. Bouzehouane, S. Fusil, and A. Barthélémy. Mapping the spatial distribution of charge carriers in $LaAlO_3$ /$SrTiO_3$ heterostructures. *Nature Materials*, Vol. 7, p. 621, 2008.

[4] D. K. Biegelsen, F. A. Ponce, J. C. Tramontana, and S. M. Koch. Ion milled tips for scanning tunneling microscopy. *Applied Physics Letters*, Vol. 50, p. 696, 1987.

[5] G. Binnig, H. Rohrer, Ch. Gerber, and E. Weibel. Surface studies by scanning tunneling microscopy. *Phys. Rev. Lett.*, Vol. 49, pp. 57–61, Jul 1982.

[6] G. Binnig, H. Rohrer, Ch. Gerber, and E. Weibel. 7×7 reconstruction on Si(111) resolved in real space. *Phys. Rev. Lett.*, Vol. 50, pp. 120–123, Jan 1983.

[7] A. Cricenti, E. Paparazzo, M. A. Scarselli, L. Moretto, and S. Selci. Preparation and characterization of tungsten tips for scanning tunneling microscopy. *Review of Scientific Instruments*, Vol. 65, p. 1558, 1994.

[8] M. F. Crommie, C. P. Lutz, and D. M. Eigler. Confinement of electrons to quantum corrals on a metal surface. *Science*, Vol. 262, No. 5131, pp. 218–220, 1993.

[9] T. Druga, M. Wenderoth, J. Homoth, M. A. Schneider, and R. G. Ulbrich. A versatile high resolution scanning tunneling potentiometry implementation. *Review of Scientific Instruments*, Vol. 81, p. 083704, 2010.

[10] I. Ekvall, E. Wahlström, D. Claesson, H. Olin, and E. Olsson. Preparation and characterization of electrochemically etched W tips for STM. *Measurement Science and Technology*, Vol. 10, No. 1, p. 11, 1999.

[11] A. Fujimori. Electronic structure of metallic oxides: Band-gap closure and valence control. *Journal of Physics and Chemistry of Solids*, Vol. 53, No. 12, pp. 1595 – 1602, 1992. ¡ce:title¿Special Issue Elecronic Structure and Fermiology of High-T.

[12] J. Garnaes, F. Kragh, K. A. Morch, and A. R. Tholen. Transmission electron microscopy of scanning tunneling tips. *Journal of Vacuum Science & Technology A*, Vol. 8, p. 441, 1990.

[13] T. Hagedorn, M. El Ouali, W. Paul, D. Oliver, Y. Miyahara, and Peter Grutter. Refined tip preparation by electrochemical etching and ultrahigh vacuum treatment to obtain atomically sharp tips for scanning tunneling microscope and atomic force microscope. *Review of Scientific Instruments*, Vol. 82, p. 113903, 2011.

[14] J. P. Ibe, P. P. Bey, S. L. Brandow, R. A. Brizzolara, N. A. Burnham, D. P. DiLella, K. P. Lee, C. R. K. Marrian, and R. J. Colton. On the electrochemical etching of tips for scanning tunneling microscopy. *Journal of Vacuum Science & Technology A*, Vol. 8, p. 3570, 1990.

[15] M. Imada, A. Fujimori, and Y. Tokura. Metal-insulator transitions. *Rev. Mod. Phys.*, Vol. 70, pp. 1039–1263, Oct 1998.

[16] Q.D. Jiang and J. Zegenhagen. c(6×2) and c(4×2) reconstruction of $SrTiO_3$(001). *Surface Science*, Vol. 425, pp. 343 – 354, 1999.

[17] P.C. Joshi and S.B. Desu. Structural, electrical, and optical studies on rapid thermally processed ferroelectric batio3 thin films prepared by metallo-organic solution deposition technique. *Thin Solid Films*, Vol. 300, pp. 289 – 294, 1997.

[18] D. Kan, T. Terashima, R. Kanda, A. Masuno, K. Tanaka, S. Chu, H. Kan, A. Ishizumi, Y. Kanemitsu, Y. Shimakawa, and Mikio Takano. Blue-light emission at room temperature from Ar+-irradiated $SrTiO_3$. *Nature Materials*, Vol. 4, p. 816, November 2005.

[19] M. Kawasaki, K. Takahashi, T. Maeda, R. Tsuchiya, M. Shinohara, O. Ishiyama, T. Yonezawa, M. Yoshimoto, and Hideomi Koinuma. Atomic control of the $SrTiO_3$ crystal surface. *Science*, Vol. 266, p. 1540, 1994.

[20] S. Kirkpatrick. Percolation and conduction. *Rev. Mod. Phys.*, Vol. 45, pp. 574–588, Oct 1973.

[21] C Kittel and H. Kroemer. 熱物理学. 丸善, 第 2 版, 1983.

[22] Y. Kozuka, M. Kim, C. Bell, B. G. Kim, Y. Hikita, and H. Y. Hwang. Two-dimensional normal-state quantum oscillations in a superconducting heterostructure. *Nature*, Vol. 462, p. 487, 2009.

[23] T Kubo and H Nozoye. Surface structure of srtio3(1 0 0). *Surface Science*, Vol. 542, No. 3, pp. 177 – 191, 2003.

[24] B. J. Last and D. J. Thouless. Percolation theory and electrical conductivity. *Phys. Rev. Lett.*, Vol. 27, pp. 1719–1721, Dec 1971.

[25] H. Lemke, T. Goddenhenrich, H. P. Bochem, U. Hartmann, and C. Heiden. Improved microtips for scanning probe microscopy. *Review of Scientific Instruments*, Vol. 61, p. 2538, 1990.

[26] L. Libioulle, Y. Houbion, J. ‐ M.Gilles. Very sharp platinum tips for scanning tunneling microscopy. *Review of Scientific Instruments*, Vol. 66, p. 97, 1995.

[27] F. Lichtenberg, D. Widmer, J. G. Bednorz, T. Williams, and A. Reller. Phase diagram of $LaTiO_x$: from 2D layered ferroelectric insulator to 3D weak ferromagnetic semiconductor. *ZEITSCHRIFT FÜR PHYSIK B CONDENSED MATTER*, Vol. 82, p. 211, 1991.

[28] M. Lippmaa, T. Furumochi, S. Ohashi, M. Kawasaki, H. Koinuma, T. Satoh, T. Ishida, and H. Nagasawa. High-temperature goniometer for thin film growth and ion scattering studies. *Review of Scientific Instruments*, Vol. 72, p. 1755, 2001.

[29] M. Lippmaa, M. Kawasaki, A. Ohtomo, T. Sato, M. Iwatsuki, and H. Koinuma. Observation of $SrTiO_3$ step edge dynamics by real-time high-temperature stm. *Applied Surface Science*, Vol. 130-132, No. 0, pp. 582 – 586, 1998.

[30] M. Lippmaa, N. Nakagawa, M. Kawasaki, S. Ohashi, and H. Koinuma. Growth mode mapping of SrTiO3 epitaxy. *Applied Physics Letters*, Vol. 76, p. 2439, 2000.

[31] M. Lippmaa, K. Terai, N. Nakagawa, K. Shibuya, Masashi Kawasaki, and Hideomi Koinuma. Nanostructures in oxide thin films: dots, wires, and rings. *Proc. SPIE*, Vol. 4467, p. 128, 2001.

[32] A. S. Lucier. Preparation and characterization of tungsten tips suitable for molecular electronics studies. Master's thesis, McGill University, 2004.

[33] F.l W. Lytle. X‐Ray diffractometry of low‐temperature phase transformations in strontium titanate. *Journal of Applied Physics*, Vol. 35, p. 2212, 1964.

[34] A J. Melmed. The art and science and other aspects of making sharp tips. *Journal of Vacuum Science & Technology B*, Vol. 9, p. 601, 1991.

[35] T. Mihara. Nanoscale heterointerface design. Master's thesis, Tokyo Institute of Technology, 2005.

[36] T. Mihara, K. Shibuya, T. Ohnishi, H. Koinuma, and M. Lippmaa. Transport properties of ultrathin oxide films and nanostructures. *Thin Solid Films*, Vol. 486, p. 63, 2005.

[37] F. Mohn, L. Gross, N. Moll, and G. Meyer. Imaging the charge distribution within a single molecule. *Nature Nanotechnology*, 2012.

[38] A. J. Nam, T. A. Lusby A. Teren, and A. J. Melmed. Benign making of sharp tips for STM and FIM: Pt, Ir, Au, Pd, and Rh. *Journal of Vacuum Science & Technology B*, Vol. 13, p. 1556, 1995.

[39] J. A. Noland. Optical absorption of single-crystal strontium titanate. *Phys. Rev.*, Vol. 94, pp. 724–724, May 1954.

[40] T. Ohnishi, H. Koinuma, and M. Lippmaa. Pulsed laser deposition of oxide thin films. *Applied Surface Science*, Vol. 252, p. 2466, 2006.

[41] T. Ohnishi, M. Lippmaa, et al. Pulsed laser ablation and deposition of complex oxides. *Journal of Physics: Conference Series*, Vol. 59, pp. 514–519, 2007.

[42] T. Ohnishi, K. Shibuya, M. Lippmaa, D. Kobayashi, H. Kumigashira, M. Oshima, and H. Koinuma. Preparation of thermally stable TiO_2-terminated $SrTiO_3$(100) substrate surfaces. *Applied Physics Letters*, Vol. 85, p. 272, 2004.

[43] T. Ohsawa, K. Iwaya, R. Shimizu, T. Hashizume, and T. Hitosugi. Thickness-dependent local surface electronic structures of homoepitaxial $SrTiO_3$ thin films. *Journal of Applied Physics*, 2012.

[44] A. Ohtomo, D. A. Muller, J. L. Grazul, and H. Y. Hwang. Artificial charge-modulationin atomic-scale perovskite titanate superlattices. *Nature*, Vol. 419, p. 378, 2002.

[45] A. Ohtomo, D. A. Muller, J. L. Grazul, and H. Y. Hwang. Epitaxial growth and electronic structure of $LaTiO_x$ films. *APPLIED PHYSICS LETTERS*, Vol. 80, No. 21, p. 3922, May 2002.

[46] R. Ohtsuka. Transport properties of embedded $LaTiO_3$ layers. Master's thesis, University of Tokyo, 2010.

[47] Y. Okada, T. Arima, Y. Tokura, C. Murayama, and N. Mori. Doping- and pressure-induced change of electrical and magnetic properties in the mott-hubbard insulator $latio_3$. *Phys. Rev. B*, Vol. 48, pp. 9677–9683, Oct 1993.

[48] A. Okazaki and M. Kawaminami. Lattice constant of strontium titanate at low temperatures. *Materials Research Bulletin*, Vol. 8, No. 5, pp. 545 – 550, 1973.

[49] A. I. Oliva, A. Romero G., J. L. Pe na, E. Anguiano, and M. Aguilar. Electrochemical preparation of tungsten tips for a scanning tunneling microscope. *Review of Scientific Instruments*, Vol. 67, p. 1917, 1996.

[50] L. Ottaviano, L. Lozzi, and S. Santucci. Scanning auger microscopy study of W tips for scanning tunneling microscopy. *Review of Scientific Instruments*, Vol. 74, p. 3368, 2003.

[51] U. J. Quaade and L. Oddershede. Electrochemical etching of sharp tips for stm reveals singularity. *Europhysics Letters*, Vol. 57, p. 611, 2002.

[52] M. Rozler and M. R. Beasley. Design and performance of a practical variable-temperature scanning tunneling potentiometry system. *Rev. Sci. Instrum*, Vol. 79, p. 073904, 2008.

[53] R.Wiesendanger, H. J. Güntherodt, G. Güntherodt, R. J. Gambino, and R. Ruf. Observation of vacuum tunneling of spin-polarized electrons with the scanning tunneling microscope. *Phys. Rev. Lett.*, Vol. 65, pp. 247–250, Jul 1990.

[54] D. David S., S. Fabien, D. T. Newell, and M. R. Castell. Ordering of TiO_2-based nanostructures on $SrTiO_3$(001) surfaces. *The Journal of Physical Chemistry B*, Vol. 110, No. 18, pp. 9246–9251, 2006.

[55] K. Shibuya, T. Ohnishi, M. Kawasaki, H. Koinuma, and M. LIPPMAA. Metallic $LaTiO_3$ /$SrTiO_3$ superlattice films on the SrTiO3 (100) surface. *Japanese Journal of Applied Physics*, Vol. 43, p. L1178, 2004.

[56] R. Shimizu, K. Iwaya, T. Ohsawa, S. Shiraki, T. Hasegawa, T. Hashizume, and T. Hitosugi. Atomic-scale visualization of initial growth of homoepitaxial $SrTiO_3$ thin film on an atomically ordered substrate. *ACS Nano*, Vol. 5, No. 10, pp. 7967–7971, 2011.

[57] S. Shiraki, M. Nantoh, S. Katano, and Maki Kawai. Nanoscale structural variation observed on the vicinal srtio3(001) surface. *Applied Physics Letters*, Vol. 96, p. 231901, 2010.

[58] F. Silly, D. T. Newell, and M. R. Castell. $SrTiO_3$(0 0 1) reconstructions: the (2×2) to c(4×4) transition. *Surface Science*, Vol. 600, No. 17, pp. 219 – 223, 2006.

[59] Dietrich Stauffer and A. Aharony. パーコレーションの基本原理. 吉岡書店, 2001.

[60] Y. Taguchi, T. Okuda, M. Ohashi, C. Murayama, N. Mori, Y. Iye, and Y. Tokura. Critical behavior in LTO. *Phys. Rev. B*, pp. 7917–7924, Mar 1999.

[61] Gh. Tahmasebipour, Y. Hojjat, V. Ahmadi, and A. Abdulla. Optimization of STM/FIM nanotip aspect ratio based on the taguchi method. *Int J Adv Manuf Technol*, Vol. 44, p. 80, 2009.

[62] Y. Tokura, Y. Taguchi, Y. Okada, Y. Fujishima, T. Arima, K. Kumagai, and Y. Iye. Filling dependence of electronic properties on the verge of metal˘mott-insulator transition in $Sr_{1-x}La_xTiO_3$. *Phys. Rev. Lett.*, Vol. 70, pp. 2126–2129, Apr 1993.

[63] R. Zhang and D. G. Ivey. Preparation of sharp polycrystalline tungsten tips for scanning tunneling microscopy imaging. *Journal of Vacuum Science & Technology B*, Vol. 14, p. 1, 1996.

[64] 小田垣孝. パーコレーションの科学. 裳華房, 1993.

[65] 大西剛, Mikk LIPPMAA. 酸化物薄膜成長中の rheed 強度振動. 表面科学, Vol. 28, No. 4, pp. 223–226, 2007.

[66] 西川治. 走査型プローブ顕微鏡 STM から SPM へ. 丸善, 1998.

[67] 藤森淳. 強相関物質の基礎. 内田老鶴圃, 2005.

[68] 上羽牧夫. シリーズ「結晶成長のダイナミクス」第 2 巻「結晶成長のしくみを探る-その物理的基礎」. 共立出版, 2002.

[69] 森田清三. 走査型プローブ顕微鏡　最新技術と未来予測. 丸善, 2005.

[70] 日本表面科学会. ナノテクノロジーのための走査プローブ顕微鏡. 丸善, 2002.

[71] 橋詰富博, 一杉太郎. 走査トンネル顕微鏡技術. 岩波書店, 2011.